Deep-Sea Research II 56 (2009) 2520–2536

Contents lists available at ScienceDirect

Deep-Sea Research II

journal homepage: www.elsevier.com/locate/dsr2

A biophysical NPZ model with iron for the Gulf of Alaska: Reproducing the differences between an oceanic HNLC ecosystem and a classical northern temperate shelf ecosystem

S. Hinckley [a,*], K.O. Coyle [b], G. Gibson [b], A.J. Hermann [c], E.L. Dobbins [c]

[a] Alaska Fisheries Science Center, 7600 Sand Point Way NE, Seattle, WA 98115, USA
[b] Institute of Marine Science, University of Alaska, Fairbanks, AK 99775, USA
[c] Joint Institute for the Study of the Atmosphere and Ocean, University of Washington, Box 357941, Seattle, WA 98195, USA

ARTICLE INFO

Article history:
Accepted 3 January 2009
Available online 24 March 2009

Keywords:
Biophysical model
NPZ model
Gulf of Alaska
ROMS model
Ocean ecosystems
Iron

ABSTRACT

Modeling the coastal Gulf of Alaska (CGOA) is complicated by the highly diverse physical and biological features influencing productivity and energy flow through the region. The GOA consists of the offshore oceanic environment, characterized by iron limitation, high-nutrients and low-chlorophyll. The coastal environment is consistently downwelling, with high iron levels from glacial melt water and runoff, but lower concentrations of macronutrients, and with a spring bloom, nutrient depletion cycle (low-nutrient, high-chlorophyll). Cross-shelf movement of water masses mixes coastal and oceanic ecosystem elements.

Simulations and field data indicate that the minimum model complexity necessary to characterize lower trophic-level production and biomass in the offshore and coastal regions includes 10 boxes: iron, nitrate, ammonium, small phytoplankton, large phytoplankton, small microzooplankton, large microzooplankton, small copepods, large oceanic copepods and detritus, with copepod mortality as a model closure term. We present the model structure, equations required (and initial parameters used) to simulate onshore and offshore lower trophic-level production in the Gulf of Alaska, along with the information from field data and simulations used to construct the model. We show the results of simulations with and without iron, and with and without two size classes of phytoplankton. These simulations indicate that our method of inclusion of iron works well to distinguish the coastal and the oceanic ecosystems, and that the inclusion of two size categories of phytoplankton is also necessary to generate the differences between these two ecosystems.

Published by Elsevier Ltd.

1. Introduction

GLOBEC (GLOBal Ocean ECosystems Dynamics) is an international research effort aimed at understanding how climate change and variability will affect the structure and dynamics of marine ecosystems (Fogarty and Powell, 2002). As part of this research effort, US GLOBEC has identified three regions of interest in the US, one of which is the coastal Gulf of Alaska (CGOA) (Fig. 1, Weingartner et al., 2002). It is expected that global climate change will impact the CGOA by altering freshwater runoff patterns and the intensity and frequency of storms, thus altering the magnitude and frequency of eddies, cross-shelf transport, buoyancy flow and stratification. Changes in physical conditions are predicted to alter the distribution, timing and intensity of phytoplankton production, which in turn will propagate through the food web to apex consumers (Fogarty and Powell, 2002). In an attempt to better understand the potential long-term impacts of climate on the CGOA ecosystem, GLOBEC supported a series of field studies starting in 1997 and extending through 2004 (Weingartner et al., 2002). As part of the research effort, an nutrient, phytoplankton, zooplankton (NPZ) model was developed to simulate the quantitative relationships between the physical and biological observations as expressed in the model equations, and to explore the relationships between historical and potential changes in the physical environment and lower trophic-level production. The NPZ model is embedded in a three-dimensional physical model to simulate biological production in time and space along the CGOA. In the following paper, we describe the NPZ model structure and its response to large-scale physical–chemical features in the North Pacific gyre and adjacent CGOA.

To accurately simulate conditions on the GOA shelf, the physical model must reproduce the major cross-shelf and alongshore current systems and eddies, in addition to water column stability. The NPZ model must be embedded in the

* Corresponding author. Tel.: +1 206 526 4109; fax: +1 206 526 6723.
E-mail address: sarah.hinckley@noaa.gov (S. Hinckley).

0967-0645/$ - see front matter Published by Elsevier Ltd.
doi:10.1016/j.dsr2.2009.03.003

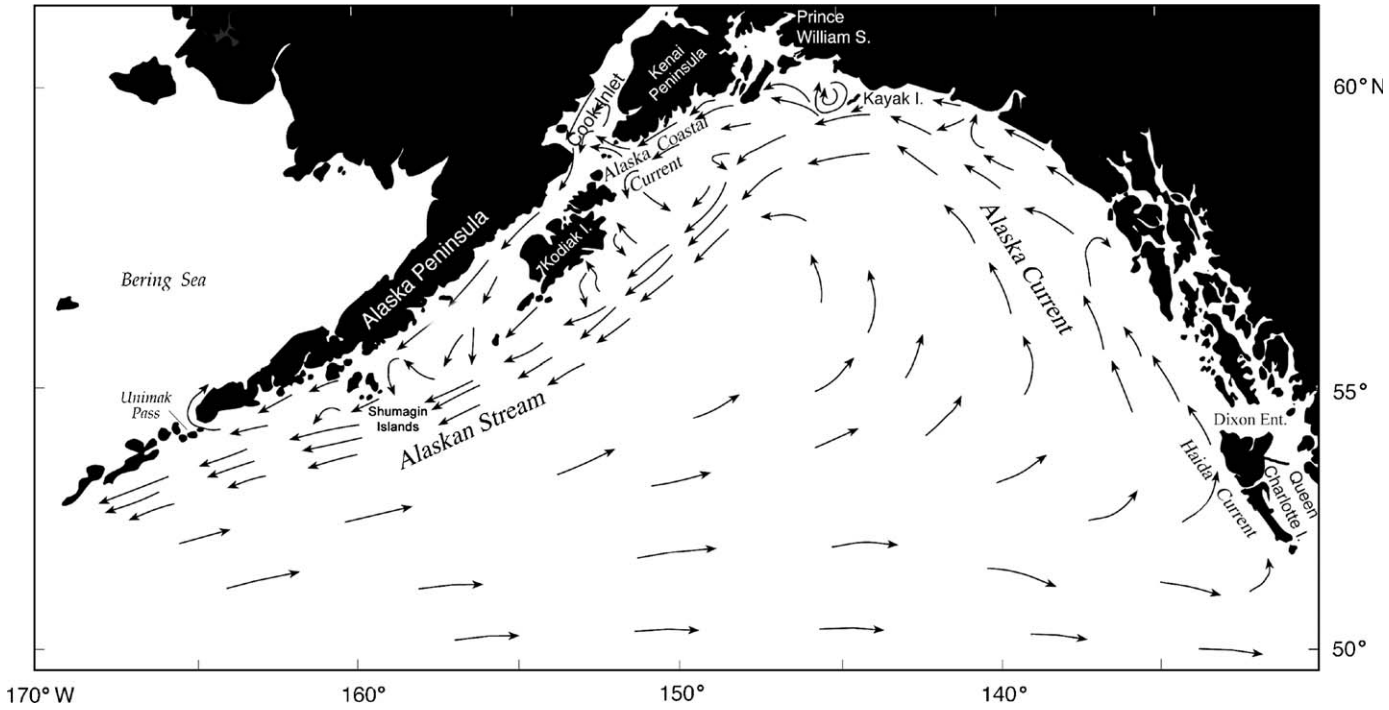

Fig. 1. Gulf of Alaska, showing major current systems. Ocean station P (50°N, 145°W) can be seen at the bottom of the figure.

physical model to simulate the biological response to the physical forcing at each location on and off the shelf. The NPZ model must be complex enough to capture the biological dynamics, but not unnecessarily complex because greater complexity requires larger numbers of parameters (Denman, 2003), greater amounts of computer time and larger storage capacity for model output. In the case of the CGOA, the NPZ model must be able to simulate the high-nutrient, low-chlorophyll (HNLC) environment in the basin and the low-nutrient, high-chlorophyll environment on the shelf (Childers et al., 2005).

The North Pacific basin, as a HNLC region, is characterized by high levels of nitrate throughout the year, and low levels of chlorophyll and no noticeable blooms (Strom et al., 2000). When it was first discovered that the basin ecosystem violates the classic seasonal cycle (Sverdrup, 1953) it was assumed that this ecosystem was controlled by top-down control in the form of mesozooplankton grazing (“The Major Grazer Hypothesis”, Miller, 1993). The assumption was that the mesozooplankton (for the most part *Neocalanus* spp.) grazed the phytoplankton faster than they could grow, so nutrients were never exhausted and phytoplankton concentrations remained constant, resulting in the observed HNLC condition. This system could be described by a simple three-box conceptual model with energy flow from nutrients to phytoplankton to the mesozooplankton.

In the 1980s, it was determined that *Neocalanus* spp. were feeding primarily on microzooplankton (Dagg and Walser, 1987) and their grazing capacity was too low by an order of magnitude to graze the phytoplankton to observed levels (Dagg, 1993). It was then hypothesized that phytoplankton were controlled by microzooplankton, which in turn were consumed by mesozooplankton. Phytoplankton at Station P in the oceanic GOA were shown to be growing at high rates (Booth et al., 1988; Welschmeyer et al., 1993); however, it was also demonstrated that the biomass and growth rates of several groups of microzooplankton were capable of controlling this production (Banse, 1982; Fenchel, 1982; Goldman and Caron, 1985; Booth, 1987). Moreover, due to the permanent halocline in this region, this relationship is not broken down by winter mixing (“The Mixing and Micrograzer Hypothesis”, Miller, 1993). Top-down control was still assumed, but now the system was described by a quasi-four-box model (nutrients, phytoplankton, herbivorous microzooplankton whose numbers are controlled by mesozooplankton predation, as illustrated by Frost (1993). Phytoplankton in the GOA can be largely divided into two size groups: small phytoplankton consisting of cyanobacteria, picoeukaryotes and nanoplankton, and large phytoplankton, consisting primarily of diatoms (E. Lessard et al., pers. commun.). Small phytoplankton form the dominant biomass across the shelf during most of the later part of the production season and are dominant at all times in the open basin. The Frost model described the annual cycle of production at Ocean Station P, and confirmed that the small-celled phytoplankton species dominant there could be held in check by microzooplankton grazers, however, this model could not account for differences in the production cycle in coastal waters (where the spring bloom largely consists of large-celled phytoplankton species, mainly diatoms) relative to the basin water (Ladd et al., 2005; Whitney et al., 2005).

The now widely known ‘Iron Hypothesis’ and the idea that iron may be limiting was first proposed by Martin and Fitzwater (1988). This hypothesis maintains that in HNLC regions the standing crop of phytoplankton is low and the net growth rate is near zero due to an inadequate supply of the micronutrient, iron to support an increase in phytoplankton biomass. If grazing was relaxed the standing crop would change a little, but if more iron was supplied the standing crop of phytoplankton would increase and nitrate would be depleted despite grazing. Several phytoplankton metabolic processes require iron (Wells et al., 1995). For example iron-containing proteins are essential for photosynthetic and respiratory electron transport; iron is also directly involved in the formation of nitrate reductase (Morel et al., 1991), the enzyme that phytoplankton use to reduce nitrate and nitrite. Iron requirements and strategies for iron acquisition differ between phytoplankton species. Temporal and spatial variations in iron

supply can therefore influence the phytoplankton biomass, production rates, size structure of the phytoplankton assemblage, species composition within size fractions, trophic dynamics and thus export production (Wells et al., 1995).

The discovery of iron depletion in the GOA basin waters (Martin and Fitzwater, 1988) led to a paradigm shift away from the idea of top-down control of phytoplankton production to one of bottom-up control by iron limitation on the growth of large cells in the basin (along with microzooplankton grazing control of small cells). Since large phytoplankton are unable to grow under iron-depleted conditions, the large phytoplankton typical of spring bloom conditions are confined mainly to coastal regions, where sufficient iron is injected with the freshwater runoff from rivers and streams, and small phytoplankton, whose growth rates are less affected by iron, are dominant in iron-depleted oceanic regions. To model both the oceanic and the coastal systems using a single comprehensive model, our conceptual model must now expand from a four-component top-down structure to a seven-box bottom-up structure consisting of small phytoplankton, large phytoplankton, microzooplankton and mesozooplankton with three additional boxes for both nitrate and ammonium (due to differential utilization by the different size categories of phytoplankton), and iron.

The GOA microzooplankton component was found to consist of two size categories, large and small, with the small microzooplankton grazing on the small phytoplankton and the large microzooplankton grazing mainly on the large phytoplankton (Strom et al., 2006, 2007). In addition, mesozooplankton comprise both large oceanic copepods such as *Neocalanus* spp., which occur in the upper mixed layer primarily in spring, and smaller neritic species such as *Pseudocalanus* spp., which occur throughout the summer (Coyle and Pinchuk, 2003, 2005). With the addition of these components and a detritus box to represent the particulate organic carbon resulting from grazing and mortality of the plankton, the model must now expand to 10 boxes. This 10-box model is the simplest conceptualization required to capture the major dynamics of the GOA ecosystem. In this paper we provide a description of the model with model equations, and present its response with and without iron to illustrate the basic model structure required to simulate both the HNLC and coastal environments. It should be noted that the parameters used here are preliminary. A complete description of model parameterization and validation will be published shortly (Coyle, K. University of Alaska, Fairbanks, Unpublished Data).

1.1. Site description

The northern GOA has a rugged mountainous coast with numerous bays, inlets and fjords. The shelf width varies, with a maximum of about 200 km and bottom depths exceed 150 m across much of the shelf. The bottom topography includes submarine canyons, ridges and submerged fjords. CGOA shelf waters are characterized by two major currents, the Alaska Current/Alaskan Stream, which flows northward/westward at or near the shelf break (Reed, 1984), and the Alaska Coastal Current, a buoyancy-driven northward/westward current within 20–50 km of shore (Fig. 1; Royer, 1982; Roach and Schumacher, 1986; Stabeno et al., 1995; Weingartner et al., 2005). Instabilities of the main currents, along with the rugged topography and strong semidiurnal tides generate numerous eddies and meanders that result in substantial cross-shelf transport of water masses (Ladd et al., 2005), and influence production as well as the distribution of nutrients and the species composition and distribution of phytoplankton and zooplankton along the shelf.

2. Methods

2.1. Physical model

To examine biophysical processes underlying productivity in the coastal GOA and the effects of climate change, a 10-compartment lower trophic-level ecosystem model (Fig. 2) was embedded in a three-dimensional regional ocean circulation model (Regional Ocean Modeling System or ROMS; Haidvogel et al., 2000). Details of the ROMS model can be found in Haidvogel et al. (2000), Moore et al. (2004) and Shchepetkin and McWilliams (2005), and on the ROMS web site (http://www.ocean-modeling.org/index.php?page=models&model=ROMS).

The ROMS ocean circulation model, as implemented for the North Pacific, consists of a series of nested grids of increasing resolution, each of which supplies initial and boundary conditions for the next finest grid (Fig. 3, Curchitser et al., 2005). The grid domains include the North Pacific (NPac) at 20–40 km resolution, the Northeast Pacific (NEP) at 10 km resolution, and the Coastal Gulf of Alaska (CGOA) at 3 km resolution. One-way nesting of the models has been implemented using a hybrid of nudging and radiation approaches (Marchesiello et al., 2001). The ocean boundaries of the CGOA domain are open, which allows entry and exit of the Alaskan Stream to and from the NEP domain. The CGOA grid has 30 vertical (sigma) levels that are concentrated near the surface. The grid's surface layer is ~0.3 m in the shallowest areas (10 m deep), and ~15 m over the basin (6000 m deep). Fig. 4 shows the relationship of sigma levels to depth across the Seward Line (Fig. 5). Bathymetry was derived from ETOPO5 and finer-scale bathymetric data. Dobbins et al. (2009) have shown that the ROMS model implemented in this region generates realistic cross-shelf water mass structure on the Seward shelf, and the seasonal cycle of vertical structure. They also show that the currents and tracer fields, and the resolution of the Alaska Coastal Current compare well with data.

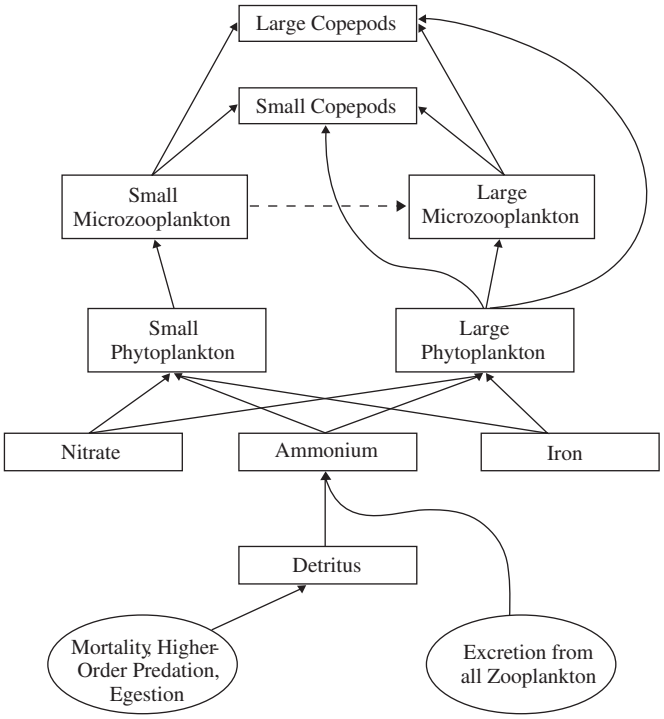

Fig. 2. Schematic representation of the GOANPZ ecosystem model. Black arrows indicate the direction of material flux. Dashed line indicates grazing by MZL on MZS, which was included in the 1D simulations only.

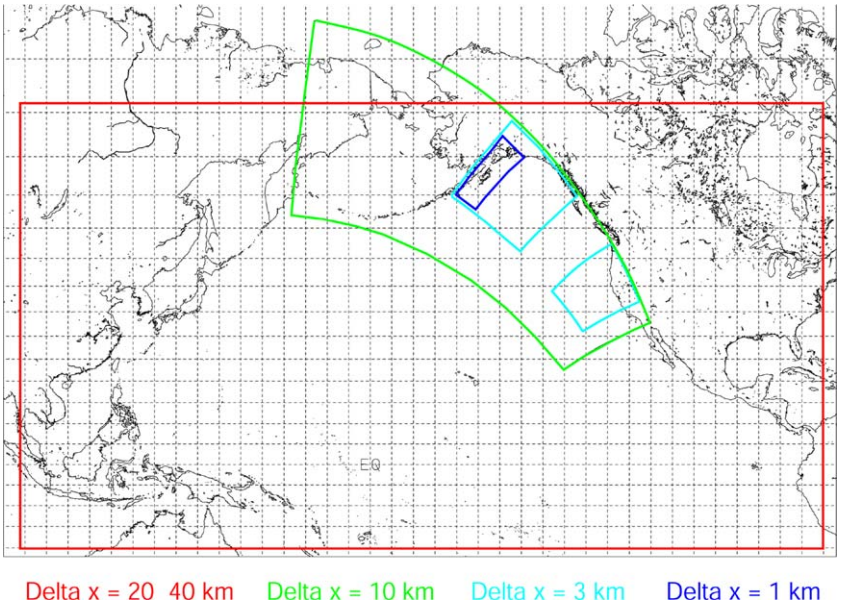

Fig. 3. Nested grids used in the ROMS model system. The NPac grid, outlined in red, has 20–40 km horizontal resolution. The NEP grid, outlined in light green, has 10 km horizontal resolution. The CGOA grid, the northernmost of the two grids outlined in light blue, has a horizontal resolution of 3 km. The GOANPZ model has been run on the NEP and the CGOA grids.

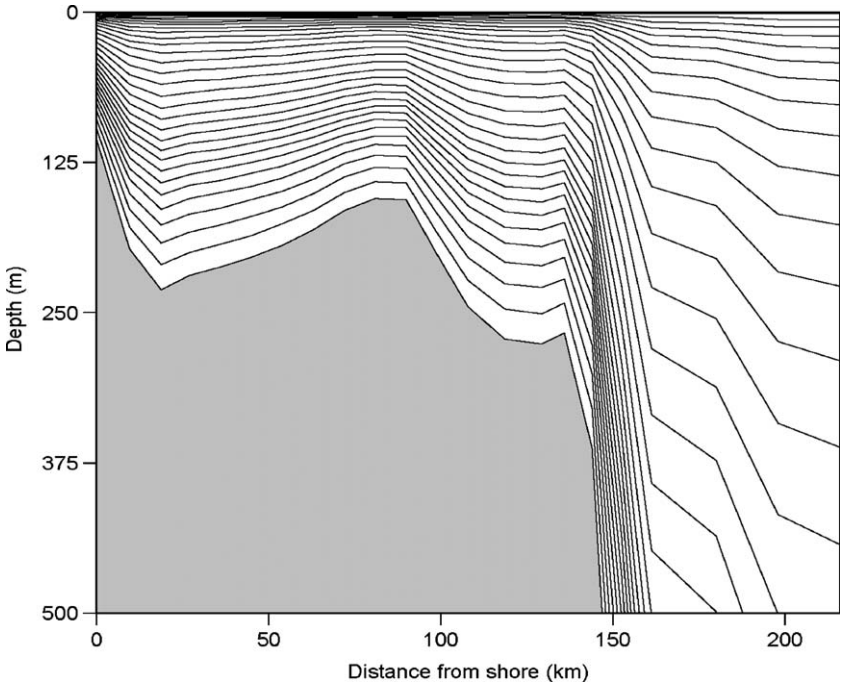

Fig. 4. Relationship between sigma levels in ROMS CGOA grid and depth in meters across the Seward Line (with the coastline on the left and the basin on the right). There are 30 sigma levels, which are compressed in shallower areas and stretched in deeper regions.

2.2. Biological model

The Gulf of Alaska nutrient–phytoplankton–zooplankton (hereafter, GOANPZ; Fig. 2) biological model contains the following state variables: nitrate, ammonium, iron, detritus, small phytoplankton ($<20\,\mu m$), large phytoplankton ($>20\,\mu m$, diatoms), small microzooplankton (heterotrophic nanoflagellates, ciliates and medium dinoflagellates), large microzooplankton (large heterotrophic dinoflagellates), small coastal copepods (represented by *Pseudocalanus* spp.), and large oceanic copepods (represented by *Neocalanus* spp.). Silicate is not included in the model at this time as nutrient data indicate that it is not limiting diatom production on the shelf (T. Whitledge, UAF, Anchorage, pers. comm.). Biological model state equations are shown in Appendix 1.

Iron was included in our NPZ model, due to iron limitation in the Alaska Gyre and its potential influence on the outer shelf and shelf break regions of the GOA. Observed iron uptake follows Michaelis–Menten kinetics (Harrison and Morel, 1986) and iron limitation has been found to reduce the concentration of reaction centers in the phytoplankton cells; iron-limited cells therefore will become light limited at lower irradiance (Greene et al., 1991).

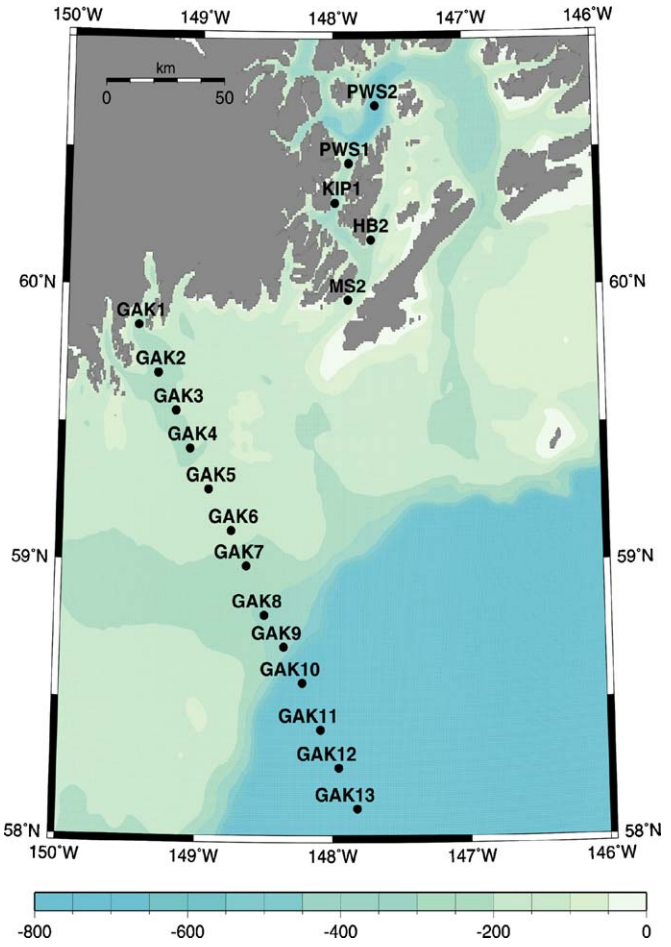

Fig. 5. Location of stations GAK 1–GAK 13 along the Seward Line on the northern Gulf of Alaska shelf.

Methods for simulating the influence of iron on the phytoplankton community vary widely, from very simple to relatively complex (Denman and Peña, 1999; Leonard et al., 1999; Chai et al., 2000; Lancelot et al., 2000; Moore et al., 2002a, b). Our model uses an intermediately complex iron regulation scheme similar to that of Fennel et al. (2003), which includes a Michaelis–Menten response of maximum photosynthetic rate to iron-deficiency, with photosynthetic efficiency increasing proportionally to the iron supply and a saturation region. Iron is not followed throughout the entire ecosystem. Iron levels are decreased proportional to small and large phytoplankton uptake, and then nudged back to the climatology, with a nudging time-scale of 30 days.

As is commonly practiced, uptake of nitrogenous nutrients follows Michaelis–Menten or Monod (1942) kinetics. We included an ammonium inhibition function in the equation that describes the growth of phytoplankton. This response reflects the fact that in the presence of ammonium, the uptake of nitrate is reduced (Wroblewski, 1977). Nitrate uptake by small (to a lesser extent) and large (to a greater extent) phytoplankton is also limited by iron. The excretion by grazers goes to ammonium, while the egested fraction goes to detritus, which is then degraded into ammonium.

Grazing by zooplankton is also modeled with a Michaelis–Menten (Ivlev, 1961; Frost, 1987) or Holling Type II functional response (Spain, 1982), modified by a Q10 factor for temperature. Prey are grazed proportionate to their abundance, modified by a feeding preference factor (fpX). Small microzooplankton were only able to graze on small phytoplankton, and large microzooplankton were able to graze on large phytoplankton alone in the 3D model, and large phytoplankton and small microzooplankton in the 1D model (see below). Small coastal copepods and large oceanic copepods could ingest large phytoplankton and both sizes of microzooplankton. Small and large phytoplankton, and small and large microzooplankton are subject to linear mortality (senescence) and sinking terms. Mesozooplankton experience linear and quadratic mortality in the 3D model and quadratic mortality alone in the 1D model. The mesozooplankton mortality factors serve as the model closure terms. Mortality of all boxes adds to the detritus term.

Subequations for processes such as maximum photosynthetic rate, photosynthetically available radiation (PAR), sinking rate of phytoplankton and detritus, and mortality of phytoplankton are shown in Appendix 2. Daily incident solar radiation at the surface is calculated as the incoming solar radiation times the density and the specific heat of seawater and a conversion factor from watts m^{-2} to Einsteins $m^{-2}\,d^{-1}$, using the algorithm of Thimijan and Heins (1983). Irradiance at depth z is computed using the extinction coefficient of seawater in a coastal region and that of phytoplankton in the water column. Photosynthetically available radiation at depth (PAR_z) is considered to equal the irradiance at depth times 0.5, as clouds are already accounted for in the daily incident solar radiation used (Frost 1987, 1993). The maximum photosynthetic rate (P_{max}) is computed using a doubling rate, which is a function of temperature. The sinking rates for small and large phytoplankton and detritus are computed as additional vertical velocities. Diapause of *Neocalanus* spp. is simulated using estimated beginning and end dates of upward movement (Day of Year (DOY) 0, DOY 60) and downward movement (DOY 156, DOY 216) as an added sinking (downward movement) or inverse sinking (rising) rate. Large oceanic copepods in the model are not subject to vertical mixing, as it is assumed that the length scales associated with their swimming is greater than those associated with vertical mixing. The linear mortality of phytoplankton is computed as a function of a critical nitrate concentration.

Parameter values for the NPZ model are shown in Appendix 3. As noted in Section 1, these parameter values are preliminary, derived from the literature, and some initial tuning and optimization, and should not be considered final. Validated model parameters will be presented in a following manuscript (Coyle, K. University of Alaska, Fairbanks, Unpublished Data).

The GOANPZ model runs from DOY 60 to DOY 270 (early March–late September) and has a time step of 0.01 d. The currency of the model is carbon (mg m^{-3}), and carbon is converted to nitrogen (mmol m^{-3}) in the nitrate and ammonium equations with a fixed conversion rate. The carbon to chlorophyll ratio was set to a constant (Frost, 1993). The biological fields are advected and diffused by the physical dynamics, as is usual in biophysical models (see Franks and Chen, 2001, Eq. (5)).

2.3. Three-dimensional model runs

The three-dimensional GOANPZ simulations described in this paper were produced by running ROMS with the embedded biological component on the 10 km NEP grid and the 3 km CGOA grid. Initial and boundary conditions for the biological variables were estimated using vertical profiles of observational data collected by the GLOBEC NEP LTOP Program on the Seward Line (Fig. 5) (http://www.ims.uaf.edu/GLOBEC/). These biological boundary conditions were constant throughout the model simulation, but due to the large geographical extent of both grids relative to the size of the GLOBEC LTOP study area, and the fast generation time of model components, boundary conditions do not appreciably affect model dynamics in the study region.

Ammonium was set to a very low initial value. Initial conditions for small phytoplankton were set to 95% of the total phytoplankton from the GLOBEC data, and those for large phytoplankton to 5% of the total, as size-fractionated biomasses were not available when this modeling was initiated. Detritus was initially set to zero at all depths. As iron was not measured as part of the GLOBEC LTOP program, where included, iron was initialized to a simple field derived from data collected by the VERTEX program (Martin et al., 1989). Iron climatology is set to 2.0 μmol/m^3 everywhere on the shelf, and 0.05–0.6 μmol/m^3 offshore (Fe_{cl}, Fig. 6). In our 3D experiments with iron, the iron field was nudged back to this original field with a time-scale equal to 30 days. This nudging serves primarily as a primitive source/sink term, which makes up for our lack of detailed knowledge regarding the dynamics of iron in this system. Note, however, that advection and diffusion of iron (both horizontal and vertical), and uptake by phytoplankton, are explicitly calculated in the dynamical model.

Two fully 3D runs of ROMS using the NEP and CGOA grids are relevant to this paper. The purpose of these runs was to illustrate the influence of iron limitation in the GOANPZ model. The first NEP simulation ran from 12/3/2000 to 11/23/2002. It was initialized with temperature, salinity, sea-surface height, and velocity from the 1996 to 2003 hindcast run of NEP described in Hermann et al. (2009). Its boundary conditions were derived from the larger NPac grid forced with NCEP atmospheric variables (Curchitser et al., 2005). Forcing was as is described in Hermann et al. (2009). Tides were not included in these simulations. The model was run twice: once with iron limitation (and nudging to iron climatology), and once with no iron limitation. Results were saved as daily averages. The second simulation, using the CGOA grid, was run for the period December 2000–2002, and details of this run may be found in Hermann et al. (2009). The modeled distribution of chlorophyll from the CGOA run for 2001 was averaged over the top 10 m and was compared with satellite monthly mean chlorophyll images.

2.4. One-dimensional model runs

Running the biological and physical model in the fully 3D grids requires large amounts of computer time. Therefore, we developed a quasi-1D (hereafter referred to as "1D") grid for use with diagnotics and testing. These 1D runs each have 30 vertical levels, stretched vertically in the same manner as for the 3D grids.

The 1D grid can be configured to represent any location in the 3D grid; bottom depth, latitude, and other qualities are appropriate to the desired location. Daily averaged physical fields (temperature, salinity, sea-surface height, and vertical eddy diffusivity) from a previously completed 3D simulation of the CGOA grid (described in Dobbins et al., 2009) were interpolated to selected Seward Line stations, and were input to each of the 1D models. This allowed biology in the 1D model to experience physical effects simulated by the fully 3D run, which included the cross-shelf advection of freshwater input at the coast and its strong impact on vertical mixing. A regional atmospheric model (MM5, see Dobbins et al., 2009) was used for surface forcing of the 3D model; vertical diffusivity was computed from the input physical fields using the KPP mixing algorithm (Large et al., 1994). Shortwave radiation from MM5 was used for light limitation terms in the 1D case.

To analyze fluxes and model structure, the 1D model was run once with iron limitation and once without iron limitation at each of the Seward Line stations (Fig. 5). We repeated these runs with the ecosystem model configured for one phytoplankton size class (parameterized as small or large cells) and with the ecosystem model configured with both large and small phytoplankton. Transect plots of model results along the Seward Line were obtained by compositing these simulations at all Seward Line (GAK) stations.

The version of the NPZ model used for the 3D and 1D experiments differed slightly due to further model development and tuning of parameters between the time the 3D and the 1D models were done (however, as noted above, both sets are still preliminary) For the 1D sensitivity experiments where iron limitation and phytoplankton size classes were manipulated, the values of the initial conditions for ammonium, both phytoplankton, both sizes of microzooplankton, and small and large copepods were all lowered. Predation (nonlinear) closure terms for the microzooplankton boxes, similar in form to that of copepods, was added. All linear mortality functions were dropped for zooplankton, so that predation was the only source of mortality for these groups. Small microzooplankton were added to the diet of large microzooplankton, based on observations from the LTOP program (E. Lessard, Univ. WA, Seattle, pers. comm.).

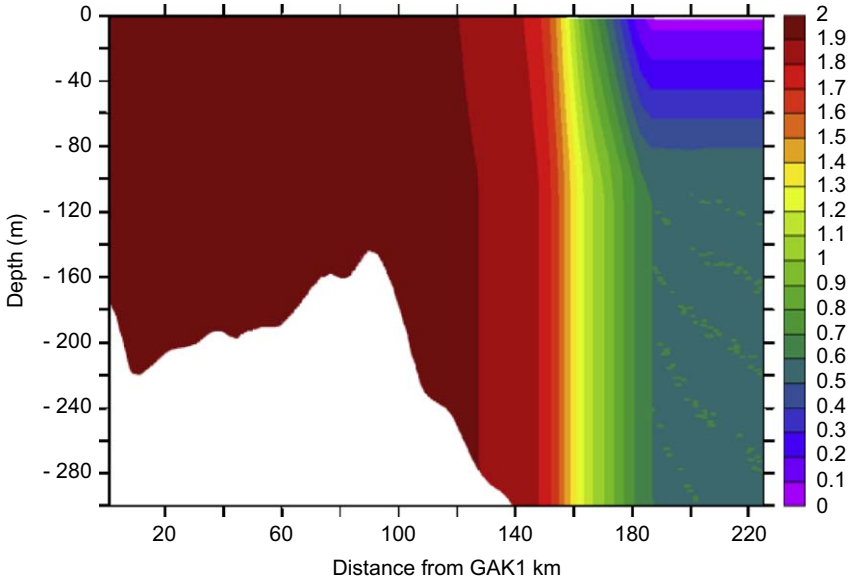

Fig. 6. Iron climatology (along the Seward Line) used in 3D simulations that included iron limitation. Contours are iron concentration (μmol m^{-3}).

Nitrogen fluxes between the biological state variables were tracked in the 1D model with the original structure and parameterization, as a cumulative sum of the concentration of nitrogen exchanged between each pair of state variables at all depths. This cumulative sum consisted of the uptake terms in the state equations for each variable. Units of flux were mmol NO m^{-3} d^{-1}. The cumulative sums were scaled relative to the maximum sum at the end of the run. The result represents a non-dimensional measure of the relative importance of each flux in a time-averaged sense for the entire run.

3. Results

3.1. Fluxes

Nitrogen fluxes (Fig. 7) were derived from the 1D model without iron, applied to the nearshore end (GAK 1), and the oceanic end (GAK 13) of the Seward Line. The simulation of the offshore station was repeated with the addition of the iron state variable and the associated iron limitation on phytoplankton growth. In the onshore areas most of the nitrogen flux was from nitrate through large phytoplankton to small copepods, with some of the large phytoplankton growth also associated with ammonium (Fig. 7A). Since GAK1 is an iron-replete region, nitrogen fluxes were not influenced by iron limitation in these simulations. Relatively small fluxes of nitrogen went through the microzooplankton compartment. Significant amounts of nitrogen flowed from the phytoplankton boxes to detritus. In the offshore area, with no iron limitation, the nitrogen flux was also mostly through large phytoplankton to copepods (Fig. 7B), similar to the flux in the coastal region. When iron limitation on the growth of phytoplankton was implemented in the 1D model of oceanic waters, the largest part of the flux went from nitrate through small phytoplankton to small microzooplankton (Fig. 7C). Nevertheless, a moderate flux of nitrogen to the large phytoplankton compartment still occurred in the simulation, as the offshore end of the Seward Line is often influenced by both oceanic and coastal regimes. Excess production of both large and small phytoplankton was transferred directly to detritus.

3.2. One-dimensional simulations of the Seward Line

A combination of large and small phytoplankton and iron limitation was required to simulate appreciable nitrate depletion over the shelf region while maintaining high-nitrate levels in the offshore region. Fig. 8 shows the cross-shelf nitrate concentrations along the Seward line simulated by applying the 1D model, with and without the iron state variable and iron limitation algorithms of phytoplankton growth in the state variable equations, and with and without large phytoplankton, to each of the Seward Line GAK stations. In the absence of large phytoplankton and iron limitation there is only a very weak draw down of nitrate across the shelf. Addition of large phytoplankton to the model resulted in a more significant depletion of nitrate across the shelf; too much nitrate drawdown occurred offshore when Fe limitation was not considered (Fig. 8, lower right panel).

Seasonal simulations, with and without iron, using only small phytoplankton produced very similar cross-shelf distributions of phytoplankton concentration (Fig. 9, left). Similar simulations with the addition of large phytoplankton produced elevated phytoplankton concentrations on the shelf during spring and early summer (Fig. 9, right). Implementation of iron limitation was required to suppress the phytoplankton biomass off the shelf. A comparison of these plots suggests that the inclusion of the two phytoplankton size classes, with different functional responses, has a stronger effect than the iron limitation factor.

Total phytoplankton concentration simulated by the 1D model in both the nearshore region (Fig. 10A) and at the offshore station (Fig. 10B) with and without iron limitation over the period March–September was examined. These results again indicate

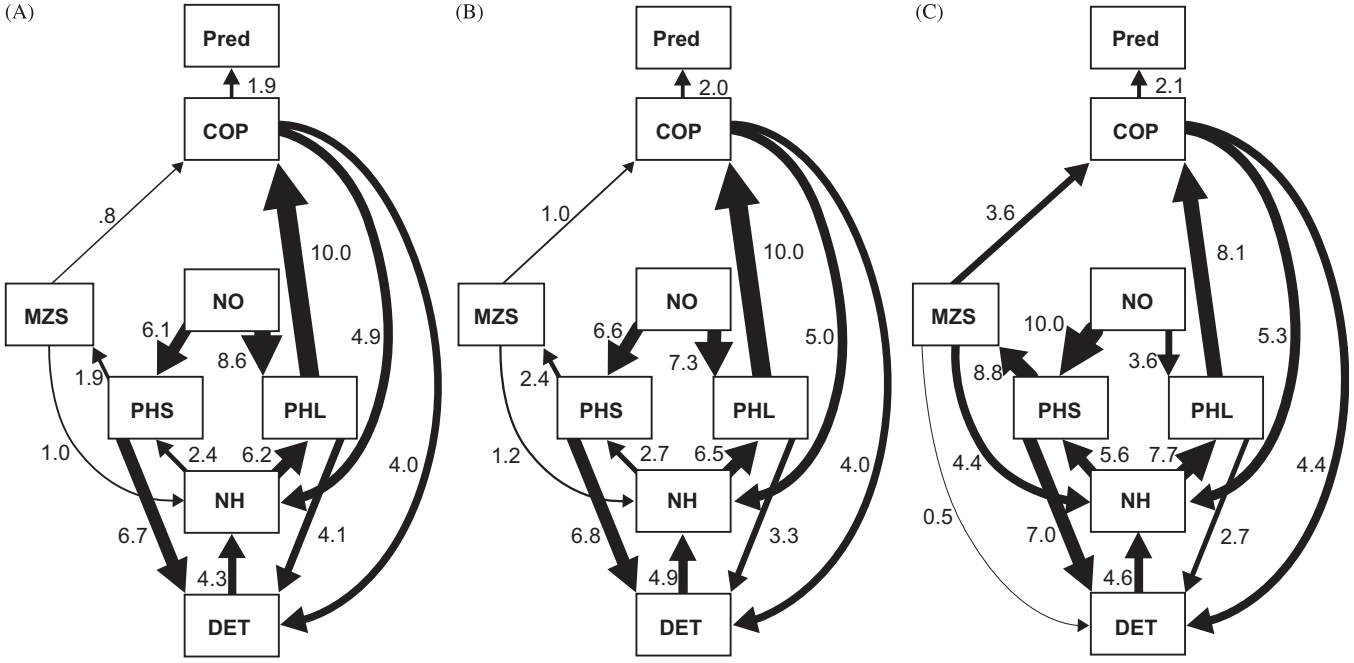

Fig. 7. Cumulative nitrate fluxes between compartments of the 1D model run at A. GAK 1 (nearshore), B. GAK 13 (offshore) without iron limitation, and C. GAK 13 with iron limitation. Symbols: DET = detritus, NH = ammonium, PHL = large phytoplankton, PHS = small phytoplankton, NO = nitrate, MZS = small microzooplankton, COP = small (neritic) copepods. Units of flux are mmol NO m^{-3} d^{-1}. For clarity, arrows for fluxes with values less than 0.5 are not shown. Note that there were no fluxes greater than 0.5 into or out of MZL, so this compartment was not shown.

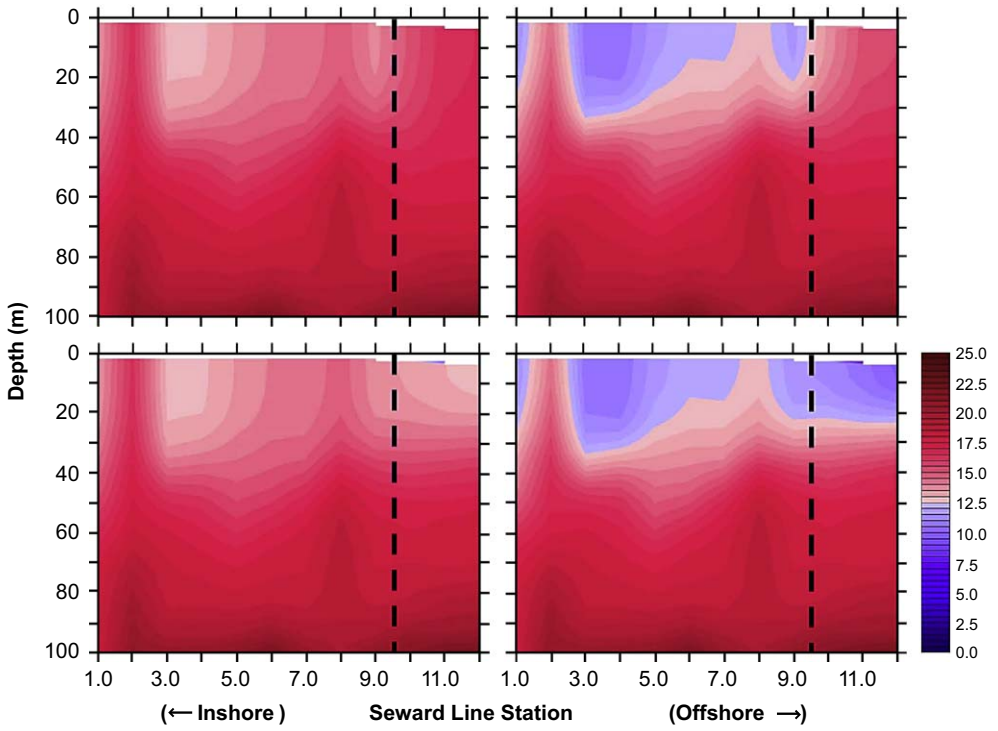

Fig. 8. Cross-shelf nitrate concentrations (mmol m^{-3}) from 1D simulations at each station on the Seward Line: small phytoplankton with iron limitation (upper left), without iron limitation (lower left); small and large phytoplankton with iron limitation (upper right), without iron limitation (lower right). Nitrate concentrations are averaged over the period March–June. Black dashed line represents the shelf break.

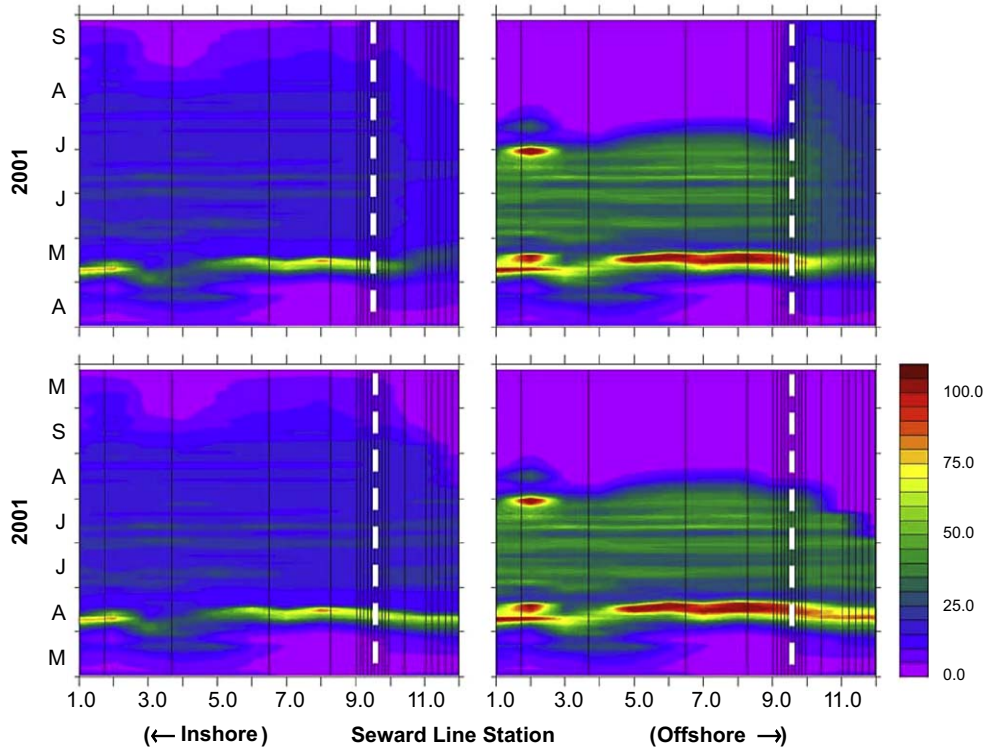

Fig. 9. Hovmuller plot of cross-shelf total phytoplankton concentrations (mg C m^{-3}), averaged over the top 10 m for March–September from the 1D simulations at each station on the Seward Line: small phytoplankton with iron limitation (upper left), without iron limitation (lower left); small and large phytoplankton with iron limitation (upper right), without iron limitation (lower right). White dashed line represents the shelf break.

that offshore iron limitation has a small effect on phytoplankton concentrations if only small phytoplankton are simulated. If both large and small phytoplankton are simulated, iron limitation offshore suppresses growth of large phytoplankton, but has little effect on the growth of small phytoplankton. In the nearshore region, implementation of iron limitation did not have a

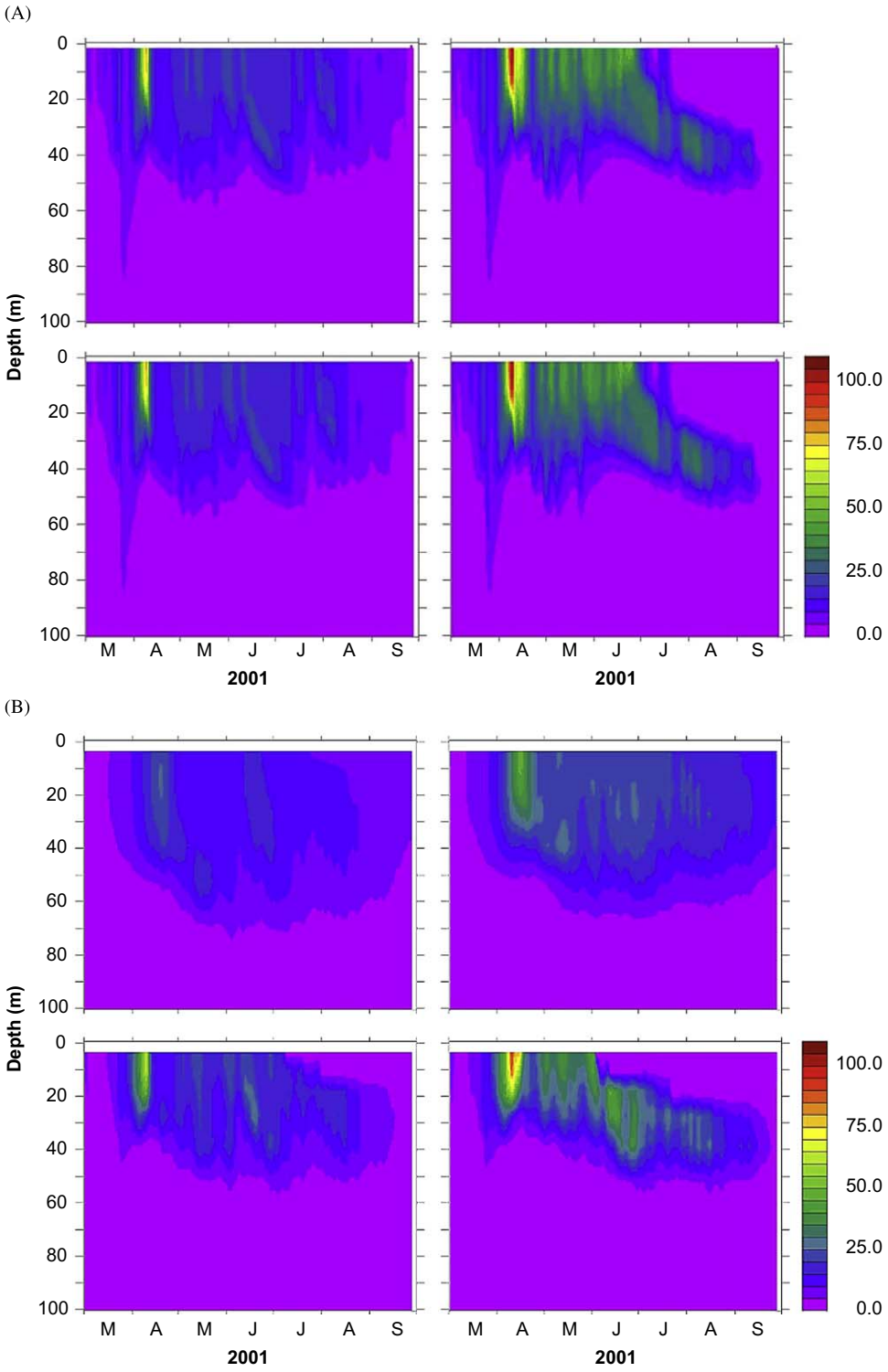

Fig. 10. (A) Total phytoplankton concentrations (mg C m^{-3}) from 1D simulations at station GAK1 on the Seward Line, over the period March–September: small phytoplankton with iron limitation (upper left), without iron limitation (lower left); small and large phytoplankton with iron limitation (upper right), without iron limitation (lower right). (B) Total phytoplankton concentrations (mg C m^{-3}) from 1D simulations at station GAK12 on the Seward Line, over the period March–September: small phytoplankton with iron limitation (upper left), without iron limitation (lower left); small and large phytoplankton with iron limitation (upper right), without iron limitation (lower right).

significant impact on the seasonal evolution of phytoplankton biomass (as this is an iron-rich region where the biomass is often dominated by large phytoplankton).

These results suggest that as currently parameterized, successful simulation of HNLC conditions offshore and low-nutrient, high-chlorophyll conditions onshore during summer requires the incorporation of two phytoplankton size classes with iron limitation. Both of these factors were necessary to produce the correct cross-shelf distribution of nitrate. Generally we observed that for the offshore region, the iron limitation term had a larger impact on the nitrate, while the multiple size classes have a larger impact on the total chlorophyll.

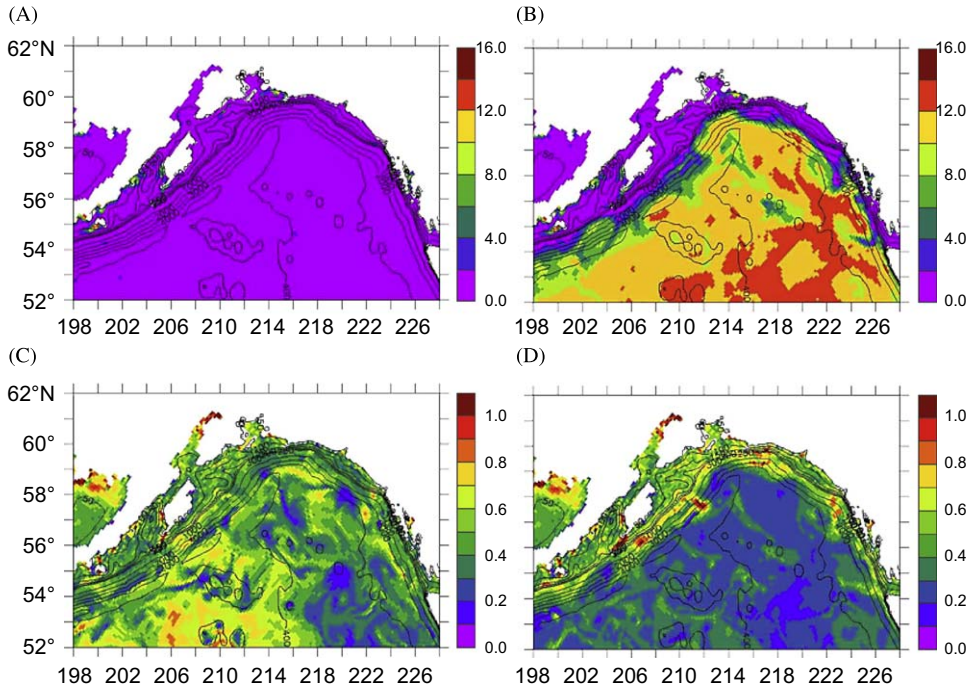

Fig. 11. Nitrate and chlorophyll fields on 11 July for model year 2001 from 3D simulations on the NEP grid. A: nitrate without iron limitation, B: with iron limitation; C: chlorophyll without iron limitation, D: with iron limitation. Nitrate fields: (mmol m^{-3}) at 10 m depth. Chlorophyll fields: (mg m^{-3}) averaged over 0–50 m depth.

3.3. *Three-dimensional simulations of Gulf of Alaska*

Three-dimensional simulations of the Gulf of Alaska without iron limitation resulted in nitrate exhaustion in the upper boundary layer over the entire grid (Fig. 11A) by early July. With iron limitation implemented, the model was able to simulate the high-nitrate condition in the offshore waters and low nitrate condition on the shelf following the spring bloom (Fig. 11B). Integrated chlorophyll in the upper mixed layer was high over the entire grid in the simulation without iron limitation (Fig. 11C) but was confined to coastal regions in the simulation with iron limitation (Fig. 11D). The model with large and small phytoplankton and iron limitation was therefore able to simulate a low-nutrient, high-chlorophyll condition for coastal waters in summer, but a high-nutrient, low-chlorophyll condition for oceanic waters.

The simulated distribution of chlorophyll over the Gulf of Alaska region compares favorably to SeaWiFS satellite images (Fig. 12) capturing the general overall trend in chlorophyll concentration during the spring and early summer. Later in the summer, the SeaWiFS images indicate substantially higher levels of chlorophyll in the inshore region than the model simulation.

4. Discussion

Although we detected discrepancies between the model results and the chlorophyll data, such discrepancies between SeaWiFS and model simulations are to be expected. SeaWiFS tends to provide higher estimates of chlorophyll than fluorometric analysis of discrete shipboard samples (Pegau and Potter, 2004). A well-known problem with SeaWiFS data, particularly in the nearshore region, is its inability to distinguish between turbidity and chlorophyll given that it only sees ocean color. Additionally the depth of the water column that is 'integrated' in a SeaWiFS image is highly dependant on the clarity of the water. Along the Gulf of Alaska coast there are numerous point sources of river input, the largest being the Copper River. The influx of sediment and glacial flour along the coast is likely to lead to an overestimate of chlorophyll in the nearshore region in SeaWiFS data. In the open ocean the compounding effect of sediment is less of a problem, but due to the greater clarity of the water, it is possible that the SeaWiFS data for this region represents chlorophyll integrated over depths greater than the 10 m used to average the model data.

Although it is possible that the satellite estimates of chlorophyll are high, it is also possible that the model does underestimate chlorophyll in some areas and times, particularly in the surface waters over the shelf after the main spring bloom. This could be due to the production by the physical model of a thin layer of low salinity water in these regions, which causes the stratification to be overestimated and reduces mixing of nutrients from the lower layers (Coyle, K. University of Alaska, Fairbanks, Unpublished Data). For example, nitrate values over the shelf near the Seward Line from the full 3D model with iron limitation were 0–2 mmol m^{-3} averaged over 0–50 m. At about the same time (midsummer) nitrate levels from a nitrate meter at 16 m on a mooring at GAK 5 were 2–5 mmol m^{-3} with spikes as high as 8 mmol m^{-3} (N. Bond, Univ. Wash./NOAA, Seattle, pers. comm.). This is a problem that the physical modelers are presently attempting to solve. However, it should be noted that Fig. 12 does only show the chlorophyll averaged over the top 10 m from model and satellite data. After May, depth-resolved data from Seward Line cruises show that the surface layer is often depleted of nutrients, and that a chlorophyll maximum layer is found at about 15–20 m (Childers et al., 2005). The 0–10 m surface layer from these data indeed shows chlorophyll levels near zero, as the model shows.

Iron concentrations offshore in the Gulf of Alaska are fairly constant at 0.6–0.7 nmol kg^{-1} (= μmol m^{-3}), but as the Alaska continental margin is approached levels almost double and are especially high near the shelf break where they exceed 1.5 nmol kg^{-1} due to plumes of iron-rich particulates (Martin et al., 1989). It has been proposed (Stabeno et al., 2004; Ladd et al., 2005) that this spatial variability in iron distribution across the GOA is

responsible for the difference in the biological regimes observed on and off the shelf, i.e. HNLC in the oceanic basin waters and the reverse, a low-nutrient, high-chlorophyll region closer to shore. Using a coupled ROMS-NPZ ecosystem model for the GOA region, we have shown that two phytoplankton size classes, and iron limitation on phytoplankton growth are both necessary to successfully simulate the HNLC condition in the Gulf of Alaska basin, while retaining a low-nutrient, high-chlorophyll regime in the coastal regions.

Small autotrophic prokaryotes (such as picoplankton) have a higher iron cell quota than large eukaryotes such as diatoms, which require only a hundredth as much (Brand, 1991). Paradoxically, the small phytoplankton are more capable of meeting their cellular energy demands for iron in low iron environments. This is thought to be because the smaller cells have a larger surface area to volume ratio and a thinner cell wall, both of which enhance iron uptake rates (Morel et al., 1991; DiTullio et al., 1993; Sunda and Huntsman, 1997).

Consequently when iron is scarce, the dominant smaller cells grow more rapidly than larger cells. Since large phytoplankton are unable to grow under iron-depleted conditions, the large phytoplankton typical of spring bloom conditions are confined mainly to coastal regions, where sufficient iron is injected with the copious freshwater runoff from rivers and streams. Small phytoplankton, whose growth rates are less affected by iron, generally dominate in iron-depleted oceanic regions.

The use of two phytoplankton groups in a marine ecosystem model is not new. It is in fact becoming the norm in large-scale ocean ecosystem modeling studies (Christian et al., 2002a, b; Moore et al., 2002a, b) in efforts to reflect our evolving

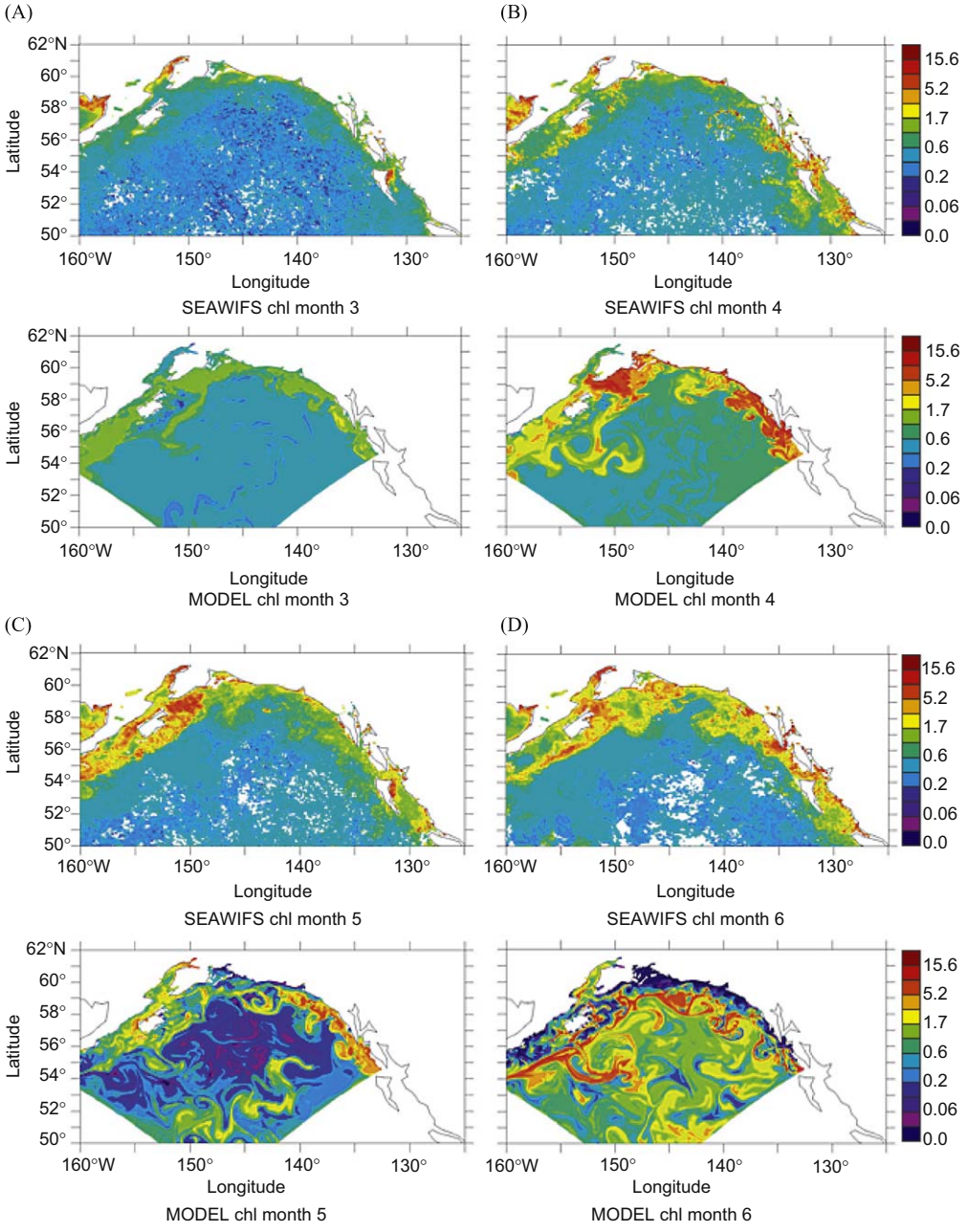

Fig. 12. Satellite ("SEAWIFS") monthly mean chlorophyll fields (first, third and fifth rows) compared with GOANPZ model chlorophyll fields (small plus large phytoplankton, averaged over the top 10 m, second, fourth and sixth rows) for A. March, B. April, C. May, D. June, E. July and F. August for 2001. Model runs for this comparison were made on the CGOA grid. Chlorophyll maps courtesy of Andrew Thomas (U. Maine, Orono).

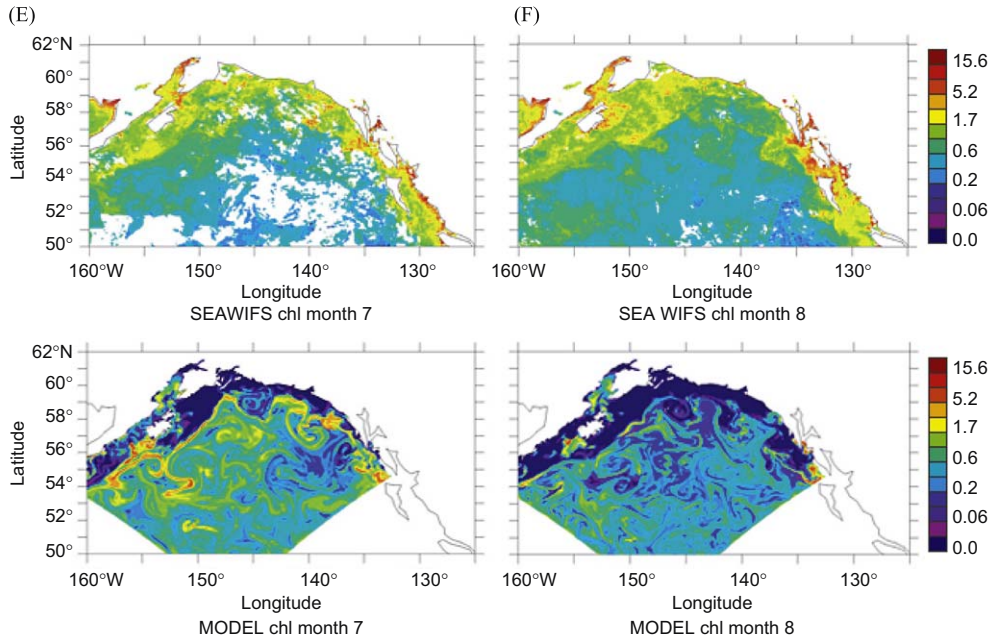

Fig. 12. (*Continued*)

understanding of the ecosystem and simulate the observed plankton community dynamics. For example, the temporal progression from large to small phytoplankton cells as the season progresses along with the differential spatial distribution of these size classes involves the use of more than one phytoplankton group. However, implementation of two phytoplankton groups in ecosystem models developed for the Gulf Alaska Region is not common. Gibson et al. (2005) did include both a large and small phytoplankton group in a 1D model developed for the CGOA for the purposes of a stability analysis. However, a 1D model developed for the Shelikof Strait (Hinckley et al., 2009) and several 1D models developed for Ocean Station P (Frost, 1987; Frost, 1993; Denman and Peña, 1999; Kawamiya et al., 1995) include only one phytoplankton component. Kawamiya et al. (2000a, 2000b) performed model simulations with their ecosystem model embedded in an ocean general circulation model for the entire North Pacific. This model had a horizontal resolution of 2°, and so while it captured the general trend of higher nitrate in the GOA basin than in the coastal region, the oceanic nitrate concentrations were somewhat low, and the resolution of the model was inadequate to determine cross-shelf patterns in nitrate and chlorophyll. More recently, Denman and Peña (2002) developed a model for Ocean Station Papa (OSP) that considered the evolution of two phytoplankton groups, although not as independent state variables; rather, the small and large phytoplankton were partitioned according to the total phytoplankton biomass.

With an increase in the awareness of the importance of iron as a limiting factor in phytoplankton growth, addition of iron to marine ecosystem models has become more common (Kawamiya, 2002). The approach to incorporating iron has varied widely in complexity from very simple (Denman and Peña, 1999; Chai et al., 2000) to relatively complex (Leonard et al., 1999; Lancelot et al., 2000; Christian et al., 2002a, b; Moore et al., 2002a, b). Although iron is known to be a limiting factor on phytoplankton growth in the oceanic Gulf of Alaska, iron has not been explicitly included as a state variable in previous models for this region. Denman and Peña (1999, 2002) previously included the effects of iron limitation on phytoplankton growth in their 1D NPZ models for OSP, but the approach taken in their modeling was to use a constant value for iron limitation, and assume that only one factor, i.e. nitrogen limitation, light limitation or iron limitation, would limit phytoplankton growth at any one time. The approach used in the present modeling study, simulating iron dynamics explicitly as a state variable, falls into an intermediately complex category. Here the effect of iron limitation was dependent upon the concentration of iron; iron concentration varied spatially and temporally, depending on the initial conditions, which were set to simulate the observed offshore–onshore gradient, advection and diffusion, uptake by phytoplankton at each time step, and nudging of this variable back to prescribed climatological conditions. This approach permitted us to achieve our goal to simultaneously simulate both the iron-rich shelf community dominated by large diatoms and the offshore iron-limited community dominated by small phytoplankton with one model configuration.

Previous modeling efforts to replicate the HNLC regime near Ocean Station P (Frost 1987, 1993; Kawamiya et al., 1995; Denman and Peña, 1999; Denman et al., 2006) used 1D models that simulated phytoplankton growth with depth and time. Frost (1993) simulated the HNLC dynamics by imposing top-down control by microzooplankton grazing on the single phytoplankton size class. In that study, Frost prescribed values of mixing and the mixed-layer depth, thus effectively determining how the ecosystem will evolve through the season. To improve upon this, Kawamiya et al. (1995) used a mixed-layer model that calculated vertical mixing and developed seasonal temperatures that matched observations. Both Frost and Kawamiya were able to reproduce the most characteristic feature of phytoplankton variation at station P—that no pronounced phytoplankton bloom takes place. However, due to the complexity of coupled physical–NPZ models it becomes difficult to attribute the whole model behavior to a specific process—biological or physical (Denman, 2003). We suggest that these models succeeded by using a parameterization for 'phytoplankton' that represented phytoplankton's ability to grow under iron-poor conditions, balanced with zooplankton grazing. Maintaining such a parameterization, it

is unlikely that these models would also be able to capture the dynamics of the phytoplankton communities in the coastal region. More recently Denman et al. (2006) used a 1-D model to replicate an iron-fertilization experiment near Ocean Station P. They found that after careful tuning their model was able to replicate 'normal' and 'fertilized' conditions with one parameter set.

Oceanic chemistry of iron and its inorganic speciation is complex, and not adequately understood (Bruland et al., 1991). This is due to the relative ease with which it can change between the valence states, Fe(II) and Fe(III), and due to the dependence of the states and their reactivity, upon the ambient hydrological, physicochemical and biological environment. Before iron can be used by phytoplankton it must dissolve in seawater (Duce and Tindale, 1991; Morel et al., 1991). However, dissolved iron exists in seawater in several different forms, and the availability of iron to phytoplankton is largely dependent upon its chemical speciation and is therefore a strong function of its redox chemistry (Bruland et al., 1991; Sunda and Huntsman, 1997). Iron availability also depends on the preference of the phytoplankton for the different forms, iron demand and uptake kinetics of a given organism, and on the reaction kinetics of iron exchange among the chemical species (Wells et al., 1995). In this modeling effort we have only considered a generic 'iron' box and not begun to consider the full iron dynamics and the potential influence of iron speciation. At present, due to the difficulty of measuring iron concentrations in the ocean (Martin et al., 1989) there is barely sufficient data to adequately initialize this variable in the model let alone constrain transfer rates among iron species, so it would seem inappropriate to attempt simulation of the various phases of iron. Such an approach, however, may become more important in light of a warming ocean and changing redox chemistry.

Archer et al. (1993) found that the horizontal advection of salt and micronutrients contributes significantly to the local load balance at OSP (in Denman and Peña, 1999). It is therefore important to simulate the physical processes as accurately as possible. 1D models do not include the effects of horizontal advection and so may give an unrealistic picture of biological–physical interactions. The approach taken here was to develop both a quasi-1D model and a fully 3D model. By using the quasi-1D model, the biology was able to experience physical effects that are as similar as possible to the fully 3D run, but without the associated computational expense. The three-dimensional model was able to simulate more complex patterns, for example eddies and onshore–offshore flow. By embedding the GOANPZ model in an ocean circulation model (ROMS), we were able to simulate the ecological dynamics across the Gulf of Alaska at a significantly higher resolution than past modeling efforts in this area. Because we are simulating, rather than prescribing the physical environment, we have developed a model that will allow in-depth exploration of ecosystem behavior in response to variability in the physical environment.

Acknowledgments

This is contribution no. 601 to the US GLOBEC program, jointly funded by the National Science Foundation and National Oceanic and Atmospheric Administration, and is contribution EcoFOCI-G660 to Fisheries-Oceanography Coordinated Investigations.

Appendix 1. Governing equations for the biological model. Advection and diffusion terms are not included, for clarity.

State variable	Equation
Nitrate (NO_3)	$\frac{\partial NO_3}{\partial t} = -\xi\left[PS\cdot P_{MAX}\left(1-e^{\left(-\frac{\alpha_{PS}PAR_z}{PMAX^*}\frac{d_{fePS}+FE}{FE}\left(\frac{d_{fePS}+2}{2}\right)\right)}\right)\left(\frac{NO_3 e^{-\Psi_{PS}NH_4}}{d_{1PS}+NO_3}\right)\left(\frac{FE}{d_{fePS}+FE}\right)\left(\frac{d_{fePS}+2}{2}\right)\right.$ $\left.+PL\cdot P_{MAX}\left(1-e^{\left(-\frac{\alpha_{PL}PAR_z}{PMAX^*}\frac{d_{fePL}+FE}{FE}\right)}\right)\left(\frac{NO_3 e^{-\Psi_{PL}NH_4}}{d_{1PL}+NO_3}\right)\left(\frac{FE}{d_{fePL}+FE}\right)\right]$
Ammonium (NH_4)	$\frac{\partial NH_4}{\partial t} = -\xi\left[\left(PS\cdot P_{MAX}\left(1-e^{\left(-\frac{\alpha_{PS}PAR_z}{PMAX^*}\frac{d_{fePS}+FE}{FE}\left(\frac{d_{fePS}+2}{2}\right)\right)}\right)\left(\frac{NH_4}{d_{2PS}+NH_4}\right)\right.\right.$ $\left.\left.+PL\cdot P_{MAX}\left(1-e^{\left(-\frac{\alpha_{PL}PAR_z}{PMAX^*}\frac{d_{fePL}+FE}{FE}\left(\frac{d_{fePL}+2}{2}\right)\right)}\right)\left(\frac{NH_4}{d_{2PL}+NH_4}\right)\right)\right.$ $+k_{MZS}e_{MZS}\left(Q_{10MZS}^{\frac{Temp-Q_{10MZST}}{10}}\right)\left(\frac{fp_{PSMZS}PS}{f_{MZS}+fp_{PSMZS}PS}\right)MZS$ $+k_{MZL}e_{MZL}\left(Q_{10MZL}^{\frac{Temp-Q_{10MZLT}}{10}}\right)\left(\frac{fp_{PLMZL}PL+fp_{MZSMZL}MZS}{f_{MZL}+fp_{PLMZL}PL+fp_{MZSMZL}MZS}\right)MZL$ $+k_C e_C\left(Q_{10C}^{\frac{Temp-Q_{10CT}}{10}}\right)\left(\frac{fp_{PLC}PL+fp_{MZSC}MZS+fp_{MZLC}MZL}{f_C+fp_{PLC}PL+fp_{MZSC}MZS+fp_{MZLC}MZL}\right)C$ $+k_{NC}e_{NC}\left(Q_{10NC}^{\frac{Temp-Q_{10NCT}}{10}}\right)\left(\frac{fp_{PLNC}PL+fp_{MZSNC}MZS+fp_{MZLNC}MZL}{f_{NC}+fp_{PLNC}PL+fp_{MZSNC}MZS+fp_{MZLNC}MZL}\right)NC$ $+degrad\cdot D\Big]$ (where $Temp = {}^{\circ}C$)
Small phytoplankton (PS)	$\frac{\partial PS}{\partial t} = PS\cdot P_{MAX}\left(1-e^{\left(-\frac{\alpha_{PS}PAR_z}{PMAX^*}\frac{d_{fePS}+FE}{FE}\frac{2}{d_{fePS}+2}\right)}\right)$ $\cdot\left(\left(\frac{NO_3 e^{-\Psi_{PS}NH_4}}{d_{1PS}+NO_3}\right)\left(\frac{FE}{d_{fePS}+FE}\right)\left(\frac{d_{fePS}+2}{2}\right)+\left(\frac{NH_4}{d_{2PS}+NH_4}\right)\right)$ $-e_{MZS}\left(Q_{10MZS}^{\frac{Temp-Q_{10MZST}}{10}}\right)\left(\frac{fp_{PSMZS}PS}{f_{MZS}+fp_{PSMZS}PS}\right)MZS$ $-m_{PS}PS-S_{PS}PS$

Large phytoplankton (*PL*)

$$\frac{\partial PL}{\partial t} = PL \cdot P_{MAX}\left(1 - e^{\left(-\frac{\alpha_{PL}\,PAR_z}{PMAX^*}\frac{d_{fePL}+FE}{FE}\frac{2}{d_{fePS}+2}\right)}\right)$$
$$\cdot\left(\left(\frac{NO_3 e^{-\Psi_{PL}NH_4}}{d_{1PL}+NO_3}\right)\left(\frac{FE}{d_{fePL}+FE}\right)\left(\frac{d_{fePL}+2}{2}\right)+\left(\frac{NH_4}{d_{2PL}+NH_4}\right)\right)$$
$$-e_{MZL}\left(Q_{10MZL}^{\frac{Temp-Q_{10MZLT}}{10}}\right)\left(\frac{fp_{PLMZL}PL}{f_{MZL}+fp_{PLMZL}PL+fp_{MZSMZL}MZS}\right)MZL$$
$$-e_C\left(Q_{10C}^{\frac{Temp-Q_{10CT}}{10}}\right)\left(\frac{fp_{PLC}PL}{f_C+fp_{PLC}PL+fp_{MZSC}MZS+fp_{MZLC}MZL}\right)C$$
$$-e_{NC}\left(Q_{10NC}^{\frac{Temp-Q_{10NCT}}{10}}\right)\left(\frac{fp_{PLNC}PL}{f_{NC}+fp_{PLNC}PL+fp_{MZSNC}MZS+fp_{MZLNC}MZL}\right)NC$$
$$-m_{PL}PL - S_{PL}PL$$

Small micro-zooplankton (*MZS*)
(Note: Mortality term nonlinear in 1D experiments, $m_{predMZS}MZS^2$)

$$\frac{\partial MZS}{\partial t} = \gamma_{MZS}e_{MZS}\left(Q_{10MZS}^{\frac{Temp-Q_{10MZST}}{10}}\right)\left(\frac{fp_{PSMZS}PS}{f_{MZS}+fp_{PSMZS}PS}\right)MZS$$
$$-e_{MZL}\left(Q_{10MZL}^{\frac{Temp-Q_{10MZLT}}{10}}\right)\left(\frac{fp_{MZSMZL}MZS}{f_{MZL}+fp_{PLMZL}PL+fp_{MZSMZL}MZS}\right)MZL$$
$$-e_C\left(Q_{10C}^{\frac{Temp-Q_{10CT}}{10}}\right)\left(\frac{fp_{MZSC}MZS}{f_C+fp_{PLC}PL+fp_{MZSC}MZS+fp_{MZLC}MZL}\right)C$$
$$-e_{NC}\left(Q_{10NC}^{\frac{Temp-Q_{10NCT}}{10}}\right)\left(\frac{fp_{MZSNC}MZS}{f_{NC}+fp_{PLNC}PL+fp_{MZSNC}MZS+fp_{MZLNC}MZL}\right)NC$$
$$-m_{MZS}MZS$$

Large Micro-zooplankton (*MZL*)
(Note: Mortality term nonlinear in 1D experiments, $m_{predMZL}MZL^2$)

$$\frac{\partial MZL}{\partial t} = \gamma_{MZL}e_{MZL}\left(Q_{10MZL}^{\frac{Temp-Q_{10MZLT}}{10}}\right)\left(\frac{fp_{PLMZL}PL+fp_{MZSMZL}MZS}{f_{MZL}+fp_{PLMZL}PL+fp_{MZSMZL}MZS}\right)MZL$$
$$-e_C\left(Q_{10C}^{\frac{Temp-Q_{10CT}}{10}}\right)\left(\frac{fp_{MZLC}MZL}{f_C+fp_{PLC}PL+fp_{MZSC}MZS+fp_{MZLC}MZL}\right)C$$
$$-e_{NC}\left(Q_{10NC}^{\frac{Temp-Q_{10NCT}}{10}}\right)\left(\frac{fp_{MZLNC}MZL}{f_{NC}+fp_{PLNC}PL+fp_{MZSNC}MZS+fp_{MZLNC}MZL}\right)NC$$
$$-m_{MZL}MZL$$

Neritic copepods (*C*)

$$\frac{\partial C}{\partial t} = \gamma_C e_C\left(Q_{10C}^{\frac{Temp-Q_{10CT}}{10}}\right)\left(\frac{fp_{PLC}PL+fp_{MZSC}MZS+fp_{MZLC}MZL}{f_C+fp_{PLC}PL+fp_{MZSC}MZS+fp_{MZLC}MZL}\right)C$$
$$-m_C C - m_{predC}C^2$$

Oceanic copepods (Neocalanoid type, *NC*)

$$\frac{\partial NC}{\partial t} = \gamma_{NC}e_{NC}\left(Q_{10NC}^{\frac{Temp-Q_{10NCT}}{10}}\right)\left(\frac{fp_{PLNC}PL+fp_{MZSNC}MZS+fp_{MZLNC}MZL}{f_{NC}+fp_{PLNC}PL+fp_{MZSNC}MZS+fp_{MZLNC}MZL}\right)NC$$
$$-m_{NC}NC - m_{predNC}NC^2$$

Detritus (*D*)
(Note: nonlinear mortality terms, $m_{predMZS}MZS^2$ and $m_{predMZL}MZL^2$ added for 1D model, and linear mortality terms for copepods dropped)

$$\frac{\partial D}{\partial t} = (1-\gamma_{MZS})e_{MZS}\left(Q_{10MZS}^{\frac{Temp-Q_{10MZST}}{10}}\right)\left(\frac{fp_{PSMZS}PS}{f_{MZS}+fp_{PSMZS}PS}\right)MZS$$
$$+(1-\gamma_{MZL})e_{MZL}\left(Q_{10MZL}^{\frac{Temp-Q_{10MZLT}}{10}}\right)\left(\frac{fp_{PLMZL}PL+fp_{MZSMZL}MZS}{f_{MZL}+fp_{PLMZL}PL+fp_{MZSMZL}MZS}\right)MZL$$
$$+(1-\gamma_C)e_C\left(Q_{10C}^{\frac{Temp-Q_{10CT}}{10}}\right)\left(\frac{fp_{PLC}PL+fp_{MZSC}MZS+fp_{MZLC}MZL}{f_C+fp_{PLC}PL+fp_{MZSC}MZS+fp_{MZLC}MZL}\right)C$$
$$+(1-\gamma_{NC})e_{NC}\left(Q_{10NC}^{\frac{Temp-Q_{10NCT}}{10}}\right)\left(\frac{fp_{PLNC}PL+fp_{MZSNC}MZS+fp_{MZLNC}MZL}{f_{NC}+fp_{PLNC}PL+fp_{MZSNC}MZS+fp_{MZLNC}MZL}\right)NC$$
$$+m_{PS}PS+m_{PL}PL+m_{MZS}MZS+m_{MZL}MZL+m_C C+m_{NC}NC+m_{predC}C^2+m_{predNC}NC^2$$
$$-degrad\cdot D - S_D D$$

Iron (*FE*)

$$\frac{\partial FE}{\partial t} = f_{ec}\cdot PS\cdot P_{MAX}\left(1-e^{\left(-\frac{\alpha_{PS}\,PAR_z}{PMAX^*}\frac{d_{fePS}+FE}{FE}\frac{2}{d_{fePS}+2}\right)}\right)$$
$$\cdot\left(\left(\frac{NO_3 e^{-\Psi_{PS}NH_4}}{d_{1PS}+NO_3}\right)\left(\frac{FE}{d_{fePS}+FE}\right)\left(\frac{d_{fePS}+2}{2}\right)+\left(\frac{NH_4}{d_{2PS}+NH_4}\right)\right)$$
$$+f_{ec}\cdot PL\cdot P_{MAX}\left(1-e^{\left(-\frac{\alpha_{PL}\,PAR_z}{PMAX^*}\frac{d_{fePL}+FE}{FE}\frac{2}{d_{fePL}+2}\right)}\right)$$
$$\cdot\left(\left(\frac{NO_3 e^{-\Psi_{PL}NH_4}}{d_{1PL}+NO_3}\right)\left(\frac{FE}{d_{fePL}+FE}\right)\left(\frac{d_{fePL}+2}{2}\right)+\left(\frac{NH_4}{d_{2PL}+NH_4}\right)\right)$$
$$+T_{nc}(FE-FE_{cl})$$
(where FE_{cl} = Iron climatology)

Appendix 2. Biological model process equations.

Process	Equation
Daily incident solar radiation	$I_0 = R_S\cdot\rho_0\cdot c_p\cdot cv$ where I_0 = irradiance at the surface ($E\,m^{-2}\,d^{-1}$), R_S = incoming shortwave radiation ($^\circ C\,m\,s^{-1}$), ρ_0 = mean density of seawater = $1025\,kg\,m^{-3}$, c_p = specific heat for sea water = $3985\,J\,kg^{-1}\,^\circ C^{-1}$, cv = conversion factor ($E\,m^{-2}\,d^{-1}$)($W^{-1}\,m^2$) = 0.394848

	(Thimijan and Heins, 1983)
	(where $W = J\,s^{-1}$)
Irradiance at depth	$I_z = I_0 e^{-(k_w + k_p(PS+PL))z}$ (Herman and Platt, 1983)
	(where z = depth (m))
Photosynthetically available radiation	$PAR_z = 0.5 I_z$ (Includes cloud cover, Frost, 1987, 1993)
Maximum carbon-specific photosynthetic rate [mg C (mg C)$^{-1}$ (d)$^{-1}$]	$P_{MAX} = (2^{DR} - 1)$
Maximum chlorophyll *a*-specific photosynthetic rate [mg Chl (mg C)$^{-1}$ (d)$^{-1}$]	$PMAX* = P_{\max} ccr$
Doubling rate (DR)	$DR = DiX(10)^{DpX \cdot Temp}$
	(where $X = S$ or L, for PS or PL, and $Temp = {}^{\circ}C$)
Sinking rate (S_x)	$S_x = (w_X)\frac{\partial X}{\partial z}$ where $X = PS$, PL or D
Mortality of small and large phytoplankton	$m_X = MAX\left(mX_{\min}, mX_{\max} - (mX_{\max} - mX_{\min})\frac{NO_3}{NO_{critX}}\right)$
	(where $X = PS$ or PL)

Appendix 3. Parameters for the biological model.

Parameter	Description	Value	Units
General Model Parameters			
ccr	Carbon-to-chlorophyll ratio	60.0	mg C (mg Chl)$^{-1}$
k_w	Extinction coefficient (due to seawater)	0.07 (0.03)	m^{-1}
k_p	Extinction coefficient (due to phytoplankton)	0.12	m^{-1}
ξ	Nitrogen:carbon ratio	0.0126	mmol N (mg C)$^{-1}$
f_{ec}	Iron to carbon ratio	1.667e-4	nmol Fe (mg C)$^{-1}$
T_{nc}	Nudging coefficient (1/30 d)	0.0333	d^{-1}
Small phytoplankton (PS)			
DiS	Doubling rate parameter for PS	0.851	d^{-1}
DpS	Doubling rate exponent for PS	0.0275 (1.2)	
α_{PS}	Slope of P–I curve for PS	21.0	mg C (mg chl-a)$^{-1}$ E m^{-2}
d_{fePS}	PS half-saturation constant for iron	0.3	μmol Fe m^{-3}
Ψ_{PS}	NH_4 inhibition coefficient for uptake of NO_3 by PS	3.0	
d_{1PS}	PS half-saturation constant for NO_3	0.5	mmol N m^{-3}
d_{2PS}	PS half-saturation constant for NH_4	1.0	mmol N m^{-3}
mPS_{min}	Minimum daily linear mortality rate for PS	0.01	d^{-1}
mPS_{max}	Maximum daily linear mortality rate for PS	0.085	d^{-1}
NO_{critPS}	Critical NO_3 for PS mortality	0.6	mg C m^{-3}
W_{PS}	Sinking rate for PS	0.15 (0.0)	m s^{-1}
Large phytoplankton (PL)			
DiL	Doubling rate parameter for PL	0.851	
DpL	Doubling rate exponent for PL	0.0275 (1.2)	μmol Fe m^{-3}
α_{PL}	Slope of P–I curve for PL	45.0 (10.0)	mg C (mg chl-a)$^{-1}$ Em^{-2}
d_{fePL}	PL half-saturation constant for iron	0.6	μmol Fe m^{-3}
Ψ_{PL}	NH_4 inhibition coefficient for uptake of NO_3 by PL	1.0	
d_{1PL}	PL half-saturation constant for NO_3	0.5	mmol N m^{-3}
d_{2PL}	PL half-saturation constant for NH_4	0.5 (1.0)	mmol N m^{-3}
mPL_{min}	Minimum daily (linear) mortality rate for PL	0.01	d^{-1}
mPL_{max}	Maximum daily (linear) mortality rate for PL	0.085	d^{-1}
NO_{critPL}	Critical NO_3 for PL mortality	0.2 (0.6)	mg C m^{-3}
W_{PL}	Sinking rate for PL	0.2	m d^{-1}
Small Microzooplankton (MZS)			
γ_{MZS}	Growth efficiency for MZS	0.5	
Q_{10MZS}	Q_{10} for MZS growth rate	2.3	
Q_{10MZST}	Temperature coefficient for Q_{10} for MZS growth rate	5.0	°C
e_{MZS}	MZS maximum specific ingestion rate	1.4 (3.0)	mg C (mg C)$^{-1}$ d^{-1}
f_{MZS}	Half-saturation constant for MZS grazing	50.0 (25.0)	mg C m^{-3}
fp_{PSMZS}	Feeding preference of MZS for PS	1.0	
m_{MZS}	Daily (linear) mortality for MZS	0.005	d^{-1}
$m_{predMZS}$	Daily (nonlinear) mortality for MZS	(0.001)	d^{-1}
k_{MZS}	Excretion by MZS	0.5	
Large microzooplankton (MZL)			
γ_{MZL}	Growth efficiency for MZL	0.5	
Q_{10MZL}	Q_{10} for MZL growth rate	2.0	
Q_{10MZLT}	Temperature coefficient for Q_{10} for MZL growth rate	5.0	°C
e_{MZL}	MZL maximum specific ingestion rate	1.0 (5.0)	mg C (mg C)$^{-1}$ d^{-1}
f_{MZL}	Half-saturation constant for MZL grazing	20.0 (50.0)	mg C m^{-3}
fp_{PLMZL}	Feeding preference of MZL for PL	1.0	
fp_{MZSMZL}	Feeding preference of MZL for MZS	(1.0)	
m_{MZL}	Daily (linear) mortality for MZL	0.005	d^{-1}
$m_{predMZL}$	Daily (nonlinear) mortality for MZL	(0.001)	d^{-1}
k_{MZL}	Excretion by MZL	0.5	

Small copepods			
γ_C	Growth efficiency for C	0.45	
Q_{10C}	Q_{10} for C growth rate	1.37	
Q_{10CT}	Temperature coefficient for Q_{10} for C growth rate	5.0	°C
e_C	C maximum specific ingestion rate	2.53 (0.5)	mg C (mg C)$^{-1}$ d^{-1}
f_C	Half-saturation constant for C grazing	57.4 (10.0)	mg C m^{-3}
fp_{PLC}	Feeding preference of C for PL	1.0	
fp_{MZSC}	Feeding preference of C for MZS	0.8 (1.0)	
fp_{MZLC}	Feeding preference of C for MZL	1.0	
m_C	Daily (linear) mortality for C	0.01	d^{-1}
$mpred_C$	Daily (nonlinear) mortality for C	0.01 (0.005)	d^{-1}
k_C	Excretion by C	0.45	
Neocalanus (NC)			
γ_{NC}	Growth efficiency for NC	0.5	
Q_{10NC}	Q_{10} for NC growth rate	1.75	
Q_{10NCT}	Temperature coefficient for Q_{10} for NC growth rate	5.0	°C
e_{NC}	NC maximum specific ingestion rate	0.17 (0.5)	mg C (mg C)$^{-1}$ d^{-1}
f_{NC}	Half-saturation constant for NC grazing	45.7 (10.0)	mg C m^{-3}
fp_{PLNC}	Feeding preference of NC for PL	0.5 (1.0)	
fp_{MZSNC}	Feeding preference of NC for MZS	0.8 (1.0)	
fp_{MZLNC}	Feeding preference of NC for MZL	1.0	
m_{NC}	Daily (linear) mortality for NC	0.001	d^{-1}
$mpred_{NC}$	Daily (nonlinear) mortality for NC	0.001 (0.01)	d^{-1}
k_{NC}	Excretion by NC	0.5	
Detritus (D)			
W_D	Sinking rate for D	3.0	m d^{-1}
degrad	Degradation rate for detritus	0.04 (0.1)	d^{-1}

Parameters in parentheses under 'Value' are those used in 1D simulations.

References

Archer, D., Emerson, S., Powell, T., Wong, C.S., 1993. Numerical hindcasting of sea surface pCO_2 at Weather Station Papa. Progress in Oceanography 32, 319–351.

Banse, K., 1982. Cell volumes, maximal growth rates of unicellular algae and ciliates, and the role of ciliates in the marine pelagial. Limnology and Oceanography 27, 1059–1071.

Booth, W.E., 1987. Contribution by diatoms to marine algal host–epiphyte photosynthesis. Botanica Marina 30, 129–140.

Booth, B.C., Lewin, J., Lorenzen, C.J., 1988. Spring and summer growth rates of subarctic Pacific phytoplankton assemblages determined from carbon uptake and cell volumes estimates using epifluorescence microscopy. Marine Biology 98, 287–298.

Brand, L.E., 1991. Minimum iron requirements of marine phytoplankton and the implications for the biogeochemical control of new production. Limnology and Oceanography 36, 1756–1771.

Bruland, K.W., Donat, J.R., Hutchins, D.A., 1991. Interactive influences of bioactive trace metals on biological production in oceanic waters. Limnology and Oceanography 36, 1555–1577.

Chai, F., Lindley, S.T., Toggweiler, J.R., Barber, R.T., 2000. Testing the importance of iron and grazing in the maintenance of the high nitrate condition in the equatorial Pacific Ocean: a physical–biological model study. In: Hanson, R.B., Ducklow, H.W., Field, J.G. (Eds.), The Changing Ocean Carbon Cycle. Cambridge University Press, Cambridge, pp. 155–185.

Childers, A.R., Whitledge, T.E., Stockwell, D.A., 2005. Seasonal and interannual variability in the distribution of nutrients and chlorophyll *a* across the Gulf of Alaska shelf: 1998–2000. Deep-Sea Research II 52, 193–216.

Christian, J.R., Verschell, M.A., Murtugudde, R., Busalacchi, A.J., McClain, C.R., 2002a. Biogeochemical modelling of the tropical Pacific Ocean. I. Seasonal and interannual variability. Deep-Sea Research II 49, 509–543.

Christian, J.R., Verschell, M.A., Murtugudde, R., Busalacchi, A.J., McClain, C.R., 2002b. Biogeochemical modelling of the tropical Pacific Ocean. II. Iron biogeochemistry. Deep-Sea Research II 49, 545–565.

Coyle, K.O., Pinchuk, P.I., 2005. Seasonal cross-shelf distribution of major zooplankton taxa on the northern Gulf of Alaska shelf relative to water mass properties, species depth preferences and vertical migration behavior. Deep-Sea Research II 52, 217–245.

Coyle, K.O., Pinchuk, P.I., 2003. Annual cycle of zooplankton abundance, biomass and production on the northern Gulf of Alaska shelf, October 1997 through October 2000. Fisheries Oceanography 12, 327–338.

Curchitser, E.N., Haidvogel, D.B., Hermann, A.J., Dobbins, E.L., Powell, T.M., Kaplan, A., 2005. Multi-scale modeling of the North Pacific Ocean: assessment and analysis of simulated basin-scale variability (1996–2003). Journal of Geophysical Research C: Oceans 110 (C11).

Dagg, M., 1993. Grazing by the copepod community does not control phytoplankton production in the subarctic Pacific Ocean. Progress in Oceanography 32, 63–183.

Dagg, M.J., Walser Jr., W.E., 1987. Ingestion, gut passage, and egestion by the copepod *Neocalanus plumchrus* in the laboratory and in the subarctic Pacific Ocean. Limnology and Oceanography 32, 178–188.

Denman, K.L., 2003. Modelling planktonic ecosystems: parameterizing complexity. Progress in Oceanography 57, 429–452.

Denman, K.L., Peña, M.A., 2002. The response of two coupled one-dimensional mixed layer/planktonic ecosystem models to climate change in the NE subarctic Pacific Ocean. Deep-Sea Research II 49, 5739–5757.

Denman, K.L., Peña, M.A., 1999. A coupled 1-D biological/physical model of the northeast subarctic Pacific Ocean with iron limitation. Deep-Sea Research II 46, 2877–2908.

Denman, K.L., Voelker, C., Peña, M.A., Rivkin, R.B., 2006. Modelling the ecosystem response to iron fertilization in the subarctic NE Pacific: the influence of grazing, and Si and N cycling on CO_2 drawdown. Deep-Sea Research II 53, 2327–2352.

DiTullio, G., Hutchins, D.A., Bruland, K.W., 1993. Interaction of iron and major nutrients controls phytoplankton growth and species composition in the tropical North Pacific Ocean. Limnology and Oceanography 38, 495–508.

Dobbins, E.L., Hermann, A.J., Stabeno, P.J., Bond, N.A., Steed, R.C., 2009. Modeled transport of freshwater from a line-source in the coastal Gulf of Alaska. Deep-Sea Research II 56 (24), 2409–2426.

Duce, R.A., Tindale, N.W., 1991. Chemistry and biology of iron and other trace metals. Limnology and Oceanography 36, 1715–1726.

Fenchel, T., 1982. Ecology of heterotrophic microflagellates. 2. Bioenergetics and growth. Marine Ecology Progress Series 8, 225–231.

Fennel, K., Abbott, M.R., Spitz, Y.H., Richman, J.G., Nelson, D.M., 2003. Impacts of iron control on phytoplankton production in the modern and glacial Southern Ocean. Deep-Sea Research II 50, 833–851.

Fogarty, M.J., Powell, T.M., 2002. Overview of the US GLOBEC Program. Oceanography 15, 4–12.

Franks, P.J.S., Chen, C., 2001. A 3-D prognostic numerical model study of the Georges Bank ecosystem. Part II: biological–physical model. Deep-Sea Research II 48, 457–482.

Frost, B.W., 1993. A modelling study of processes regulating plankton standing stock and production in the open subarctic Pacific Ocean. Progress in Oceanography 32, 17–56.

Frost, B.W., 1987. Grazing control of phytoplankton stock in the open subarctic Pacific Ocean: a model assessing the role of mesozooplankton, particularly the large calanoid copepods *Neocalanus* spp. Marine Ecology Progress Series 39, 49–68.

Gibson, G.A., Musgrave, D.L., Hinckley, S., 2005. Non-linear dynamics of a pelagic ecosystem model with multiple predator and prey types. Journal of Plankton Research 27, 427–447.

Goldman, J.C., Caron, D.A., 1985. Experimental studies on an omnivorous microflagellate: implications for grazing and nutrient regeneration in the marine microbial food chain. Deep-Sea Research 32, 899–915.

Greene, R.M., Geider, R.J., Falkowski, P.G., 1991. Effect of iron limitation on photosynthesis in a marine diatom. Limnology and Oceanography 36, 1772–1782.

Haidvogel, D.B., Arango, H.G., Hedstrom, K., Beckmann, A., Malanotte-Rizzoli, P., Shchepetkin, A.F., 2000. Model evaluation experiments in the North Atlantic Basin: simulations in nonlinear terrain-following coordinates. Dynamics Atmosphere Oceans 32, 239–281.

Harrison, G.I., Morel, F.M.M., 1986. Response of the marine diatom *Thalassiosira weissflogii* to iron stress. Limnology and Oceanography 31, 988–997.

Herman, A.W., Platt, T., 1983. Numerical modeling of diel carbon production and zooplankton grazing on the Scotian shelf based on observational data. Ecological Modeling 18, 55–72.

Hermann, A.J., Curchitser, E.N., Dobbins, E.L., Haidvogel, D.B., 2009. A comparison of remote versus local influence of El Nino on the coastal circulation of the Northeast Pacific. Deep-Sea Research II 56 (24), 2427–2443.

Hinckley, S., Napp, J.M., Hermann, A.J., Parada, C., 2009. Simulation of physically-mediated variability in prey resources of a larval fish: a three-dimensional NPZ model. Fisheries Oceanography, doi:10.1111/j.1365-2419.2009.00505.x.

Ivlev, V.S., 1961. Intensity of feeding. In: Ivlev, V.S. (Ed.), Experimental Ecology of Feeding of Fishes. Yale University Press, New Haven, p. 302.

Kawamiya, M., 2002. Numerical model approaches to address recent problems on pelagic ecosystems. Journal of Oceanography 58, 365–378.

Kawamiya, M., Kishi, M.J., Suginohara, N., 2000a. An ecosystem model for the North Pacific embedded in a general circulation model. Part I: Model description and characteristics of spatial distributions of biological variables. Journal of Marine Systems 25, 129–157.

Kawamiya, M., Kishi, M.J., Suginohara, N., 2000b. An ecosystem model for the North Pacific embedded in a general circulation model. Part II: Mechanisms forming seasonal variations of chlorophyll. Journal of Marine Systems 25, 159–178.

Kawamiya, M., Kishi, M.J., Yamanaka, Y., Suginohara, N., 1995. An ecological–physical coupled model applied to [Ocean Weather] Station Papa. Journal of Oceanography 51, 635–664.

Ladd, C., Stabeno, P., Cokelet, E.D., 2005. A note on cross-shelf exchange in the northern Gulf of Alaska. Deep-Sea Research II 52, 665–843.

Lancelot, C., Hannon, E., Becquevort, S., Veth, C., de Baar, H.J.W., 2000. Modelling phytoplankton blooms and carbon export production in the Southern Ocean: dominant controls by light and iron in the Atlantic sector in Austral spring in 1992. Deep-Sea Research I 47, 1621–1662.

Large, W.G., McWilliams, J.C., Doney, S.C., 1994. Oceanic vertical mixing—a review and a model with a nonlocal boundary-layer parameterization. Reviews of Geophysics 32, 363–403.

Leonard, C.L., McClain, C.R., Murtugudde, R., Hofmann, E.E., Harding, L.W., 1999. An iron-based ecosystem model of the central equatorial Pacific. Journal Geophysical Research 104, 1325–1341.

Marchesiello, P., McWilliams, J.C., Shchepetkin, A.F., 2001. Open boundary conditions for long-term integration of regional oceanic models. Ocean Modelling 3, 1–20.

Martin, J.H., Fitzwater, S.E., 1988. Iron deficiency limits phytoplankton growth in the north-east Pacific subarctic. Nature 331, 341–343.

Martin, J.H., Gordon, R.M., Fitzwater, S., Broenkow, W.W., 1989. VERTEX: phytoplankton/iron studies in the Gulf of Alaska. Deep-Sea Research A 36, 649–680.

Miller, C.B., 1993. Pelagic production processes in the subarctic Pacific. Progress in Oceanography 32, 1–15.

Monod, J., 1942. Recherches sur la croissance des cultures bact'eriennes [Studies on the growth of bacterial cultures]. Actualities Scientifique et Industrielles 911, 1–215.

Moore, J.K., Doney, D.M., Scott, C., Lindsay, K., 2004. Upper ocean ecosystem dynamics and iron cycling in a global three-dimensional model. Global Biogeochemical Cycles 18, GB4028.

Moore, J.K., Doney, S.C., Glover, D.M., Fung, I., 2002a. Iron cycling and nutrient limitation patterns in surface waters of the world ocean. Deep-Sea Research II 49, 463–507.

Moore, J.K., Doney, S.C., Kleypas, J.A., Glover, D.M., 2002b. An intermediate complexity marine ecosystem model for the global domain. Deep-Sea Research II 49, 403–462.

Morel, F.M.M., Rueter, J.G., Price, N.M., 1991. Iron nutrition of phytoplankton and its possible importance in the ecology of ocean regions with high nutrient and low biomass. Oceanography 4, 56–61.

Pegau, S., Potter, R., 2004. Visible remote sensing in the Gulf of Alaska. Exxon Valdez Oil Spill Gulf Ecosystem Monitoring and Research Final Report, G030685.

Reed, R.K., 1984. Flow of the Alaskan Stream and its variations. Deep-Sea Research 31, 369–386.

Roach, A.T., Schumacher, J.D., 1986. Observations of the Alaska Coastal Current in Shelikof Strait, Alaska. Eos, Transactions, American Geophysical Union 67, 1042.

Royer, T.C., 1982. Coastal freshwater discharge in the Northeast Pacific. Journal of Geophysical Research 87, 2017–2021.

Shchepetkin, A.F., McWilliams, J.C., 2005. The regional ocean modeling system: a split-explicit, free-surface, topography-following coordinate ocean model. Ocean Modeling 9, 347–404.

Spain, J.D., 1982. Basic Microcomputer Models in Biology. Addison-Wesley, London.

Stabeno, P.J., Reed, R.K., Schumacher, J.D., 1995. The Alaska Coastal current: continuity of transport and forcing. Journal of Geophysical Research—Oceans 100, 2,477–2,485.

Stabeno, P.J., Bond, N.A., Hermann, A.J., Kachel, N.B., Mordy, C.W., Overland, J.E., 2004. Meteorology and oceanography of the Northern Gulf of Alaska. Continental Shelf Research 24, 859–897.

Strom, S.L., Miller, C.B., Frost, B.W., 2000. What sets lower limits to phytoplankton stocks in high-nitrate, low-chlorophyll regions of the open ocean? Marine Ecology Progress Series 193, 19–31.

Strom, S.L., Macri, E.L., Olson, M.B., 2007. Microzooplankton grazing in the coastal Gulf of Alaska: variations in top-down control of phytoplankton. Limnology and Oceanography 52, 1480–1494.

Strom, S.L., Olson, M.B., Macri, E.L., Mordy, C.W., 2006. Cross-shelf gradients in phytoplankton community structure, nutrient utilization, and growth rate in the coastal Gulf of Alaska. Marine Ecology Progress Series 328, 75–92.

Sunda, W.G., Huntsman, S.A., 1997. Interrelated influence of iron, light and cell size on marine phytoplankton growth. Nature 390, 389–392.

Sverdrup, H.U., 1953. On conditions for the vernal blooming of phytoplankton. Journal Du Conseil International pour l'Exploration de la Mer 18, 287–295.

Thimijan, R.W., Heins, R.D., 1983. Photometric, radiometry, and quantum light units measure: a review of procedures for interconversion. Hortscience 18, 818–822.

Wells, M.L., Price, N.M., Bruland, K.W., 1995. Iron chemistry in sea water and its relationship to phytoplankton: a workshop report. Marine Chemistry 48, 157–182.

Weingartner, T.J., Danielson, S.L., Royer, T.C., 2005. Freshwater variability and predictability in the Alaska Coastal Current. Deep-Sea Research II 52, 169–191.

Weingartner, T.J., Coyle, K., Finney, B., Hopcroft, R., Whitledge, T., Brodeur, R., Dagg, M., Farley, E., Haidvogel, D., Haldorson, L., Hermann, A., Hinckley, S., Napp, J., Stabeno, P., Kline, T., Lee, C., Lessard, E., Royer, T., Strom, S., 2002. The Northeast Pacific GLOBEC Program: Coastal Gulf of Alaska. Oceanography 15 (2), 48–63.

Welschmeyer, N.A., Strom, S., Goericke, R., DiTullio, G., Belvin, M., Petersen, W., 1993. Primary production in the subarctic Pacific Ocean: Project SUPER. Progress in Oceanography 32, 101–135.

Whitney, F.A., Crawford, W.R., Harrison, P.J., 2005. Physical processes that enhance nutrient transport and primary productivity in the coastal and open ocean of the subarctic NE Pacific. Deep-Sea Research II 52, 681–706.

Wroblewski, J.S., 1977. A model of phytoplankton plume formation during variable Oregon upwelling. Journal Marine Research 35, 357–394.